Final Test Guideline

PROJECT

Displacement Damage Guideline

WORK PACKAGE NUMBER

OA B O

DOCUMENT NUMBER

0195162

CUSTOMER ID NUMBER

REVISION

01.02

REVISION OR RELEASE DATE

16th May 2014

STATUS

Issued

PREPARED BY

Mark Robbins

REVIEWED BY

APPROVED BY

CUSTOMER APPROVAL

Surrey Satellite Technology Limited
Tycho House
20 Stephenson Road
Surrey Research Park
Guildford, Surrey
GU2 7YE, UK
Tel: +44 1483 803803
Fax: +44 1483 803804
Email: sstl@sstl.co.uk

TABLE OF CONTENTS

LIST OF FIGURES

LIST OF TABLES

DISTRIBUTION LIST

Name	Organisation	No. of copies	Release Date
Christian Poivey	ESA, ESTEC	Electronic	

DOCUMENT REVISION STATUS

Last Edited Date	Revision / Release Number	Status	Edited By	Pages / Paragraphs Affected	Change Ref
13/11/2012	01.00	issued	M S Robbins	All new document	
10/12/2012	01.01	issued	M S Robbins	Minor updates following final milestone meeting – Sections 1.1, 1.3, 5, 6.2, 7.4.4	
16/05/2014	01.02	issued	M S Robbins	Copyright statement removed at the request of ESA to aid distribution. Commercial in Confidence statement removed from footer	

1 INTRODUCTION

1.1 Scope

This document is intended as an input into the formal drafting of the ESCC guidelines for displacement damage testing of 2d-imagers, such as CCDs, CMOS image sensors (CIS, also known as active pixel sensors, APS, or monolithic active pixel sensors, MAPS), as well as infrared imager arrays. These types of sensors are also available in 1-D format and this guideline document will also be applicable to them.

These guidelines cover the effects of irradiation conditions, typical test measurements, discussion of radiation sources, dosimetry and planning issues. The appendices cover technical subjects of relevance to those undertaking displacement damage testing and include a discussion of the space radiation environment, modelling activities, an overview of 2d imager technology, the basic mechanisms for displacement damage and annealing behaviour and the effect of displacement damage on imager performance.

This document is deliverable D5 under ESA contract 4000101510/11/NL/NR. Device testing was also undertaken within the framework of this contract, the test report being deliverable D3 [AD-2].

1.2 Applicable Documents

Applicable Documents identified in the following text are identified by **AD-n**, where “n” indicates the actual document, from the following list:

AD#	Title	Document Number	Issue	Revision	Date
1	ESA Statement of Work	TEC_QEC/CP/SOW/2009-2	1	Rev 2	05/11/2009
2	Test Report, D3	SSTL# 0193867	1	2	23/10/12
3					

1.3 Reference Documents

Documents referenced in the following text, are identified by **RD-n**, where “n” indicates the actual document, from the following list: Reference Documents are those over which SSTL has no control, such as Outgassing Manuals, NASA Handbooks etc.

RD#	Title	Document Number	Issue	Revision	Date
1	Total Dose Steady-state Irradiation Test Method, ESCC Basic Specification 2290	22900			3/3/2007
2	MIL-STD-883G, Test Method Standard for Microcircuits, Method 1019.8 Ionizing radiation (total dose) test procedure	MIL-STD-883G			28/02/2006
3	Single Event Effects Test Method And Guidelines, ESCC Basic Specification 25100	25100			1/10/2002
4	ASTM E722-94 (Reapproved 2002), 'Standard practice for Characterizing Neutron energy Fluence Spectra in Terms of an equivalent Mono-energetic Fluence for Radiation-hardness testing of Electronics, available from ASTM website				
5	NASA NEPP document “Proton test guideline development – lessons learned”. Available from NASA GSFC Radhome website				22/08/2002

1.4 Acronyms and Abbreviations

The following abbreviations are used within this document:

	Description
ADC	Analogue to Digital Converter
ADU	Analogue to Digital Unit
APS	Active Pixel Sensor
DAC	Digital to Analogue Converter
DD	Displacement Damage
DSNU	Dark Signal Non-Uniformity
DUT	Device Under Test
E-O	Electro-Optical
HIF	Heavy Ion Facility
LET	Linear Energy Transfer
MCT	Mercury Cadmium Telluride
MNOS	Metal Nitride Oxide Semiconductor
MOS	Metal Oxide Semiconductor
MSPS	Mega Samples Per Second
PRNU	Photo Response Non-Uniformity
RMS	Root Mean Square
ROIC	Read Out Integrated Circuit
RT	Room Temperature
SEE	Single Event Effect
SEFI	Single Event Functional Interrupt
SEL	Single Event Latch Up
SEU	Single Event Upset
SOW	Statement of Work
TBC	To Be Confirmed
TBD	To Be Defined
TEC	Thermo-Electric Cooler
TID	Total Ionizing Dose

2 GENERAL INTRODUCTION

It is highly desirable to have a set of recommended test guidelines to achieve a harmonization of testing activities and subsequent interpretation of data. Such a situation has existed for some time in the areas of total ionizing dose testing (e.g. RD1 and RD2) and single event testing (e.g. RD3). However, a similar set of guidelines has never been produced for displacement damage testing. A “lessons learned” document for proton testing in general has been produced by NASA (RD5) and a standard (RD4) does exist for neutron testing, but it is not particularly relevant for space applications.

The reasons for the lack of standardisation in displacement damage testing are varied, for example

- The devices most affected by displacement damage are those that interact with, or emit, optical radiation (termed ‘photonic’ or ‘optoelectronic’ devices). These can be formed from a wide range of materials (not only silicon but also materials such as GaAs, InGaAs, HgCdTe and InSb).
- Post-irradiation annealing is often important and the timescales and temperatures involved can be specific to the device or to the type of defects involved.
- Although there is significant literature on displacement damage effects, it is not as large as that for TID and SEE, probably because of
    - A lesser technological interest
    - Difficulties in device testing (often requiring specialised optical equipment and time consuming measurements)
    - The often high cost of devices (and corresponding reduction in the number of devices tested)
    - And it appears more difficult to circumvent displacement damage effects, by design or technology choices, than TID and SEE, therefore users have learned to live with the degradation.

However, enough is now known about its effects to attempt to produce a guideline document, even if this cannot define a rigid procedure for all cases. It is the aim of this present work to provide users, at least, with an awareness of the issues and the implications of using particular test methods, for example.

The following sections discuss areas that should be considered when planning an irradiation campaign likely to involve displacement damage effects. They cover the effects of irradiation conditions, including the choice of particle type and energy, a description of radiation sources, dosimetry and a discussion of planning issues. Finally, an outline of typical test measurements and test methods is given. The appendices cover technical subjects of relevance to those undertaking displacement damage testing and include a discussion of the space radiation environment, modelling activities, an overview of 2d imager technology, the basic mechanisms for displacement damage and annealing behaviour and the effect of displacement damage on imager performance.

3 IRRADIATION CONDITIONS

When planning an irradiation campaign the conditions under which the irradiations are undertaken must be considered carefully. The main points are discussed in this section.

3.1 Particle Type and Energy

The displacement damage produced by different particles and energies is normally related through the Non-ionizing Energy Loss (NIEL). NIEL scaling seems to work reasonably well in many situations, as discussed in Appendix A6.2. However, care must be taken in choosing the irradiating particle and energy to ensure that the type of bulk defects being generated and the resultant degradation is representative of the mission. For example, degradation mechanisms that rely on the generation of defect clusters, such as RTS generating centres, may not be observed if the material is irradiated with high energy electrons, even though the electrons can cause displacement damage. If NIEL scaling is uncertain, especially for non-silicon devices, testing at several energies to confirm whether NIEL scaling holds can be useful.

Ideally, for mission evaluation, the devices under test should be irradiated with particles and energies representative of the operating environment to avoid uncertainties in the NIEL approach. By utilising a selection of proton beam degraders and sequential irradiations an approximation to the proton environment for low earth orbits has been simulated [1]. This could be particularly useful for the testing of devices where NIEL calculation and its application can be uncertain (for example II-VI materials). These degraders are currently only available at the KVI facilities at Groningen and full simulation of the environment is often not a practical proposition. Therefore the irradiations should be undertaken using the dominant particle type and energy to minimise the reliance on NIEL scaling. For example, the most common use for space-borne imagers is in moderate to well-shielded applications in low earth orbit. In these cases the main interest is in protons with energies of several tens of MeV as the shielded spectrum usually has a peak at around 50 to 60 MeV. Hence a good energy for testing is around 55 MeV. 10 MeV protons are sometimes used for convenience, because of beam availability or activation issues, for example. However, it should be noted that if dark signal distributions are important for the mission success, the use of low energy protons may not provide a good representation of mission performance (Section A6.3.2). Also, care must be taken if proton irradiations are being used for a combined test of total ionising dose (TID) and displacement damage effects. At these low energies intracolumnar recombination of the generated electron hole pairs become significant, leading to a lower degradation due to TID than would be expected if irradiating with Co^{60} gammas or higher energy protons.

Choosing an optimum energy for irradiation testing does depend on detailed knowledge of the shielding and the environment and sometimes issues can be missed. For example, the CCDs on board the Chandra Observatory experienced significantly higher than expected charge transfer degradation due displacement damage when passing through the South Atlantic Anomaly. This was traced to low energy protons (~100 keV) scattering through the x-ray optics and depositing their energy within the buried channel of the CCD. In most conventional applications of imaging arrays these low energy protons would have been prevented from reaching the device.

Neutrons are sometimes used for space simulation to avoid ionisation effects that occur when irradiating with charged particles. However, there is relatively little literature on neutron damage of CCDs and other imagers. One possible problem with neutron irradiation is that the energy spectrum is not normally mono-energetic and the dosimetry and application of NIEL can be complicated.

When undertaking fundamental studies it is desirable to know the actual energy spectrum of the particles incident on the device. Using a tuned beam to obtain mono-energetic protons is preferable to using degraders to obtain the required proton energy. Degraded beams have significant straggle in the beam energies that can complicate the data analysis. For example, the Proton Irradiation Facility (PIF) at the Paul Scherrer Institute (PSI) provide 10 MeV protons by utilising a 74.3 MeV beam reduced in energy by using 0.4 mm Aluminium and 7.5 mm Copper degraders. The resultant energy spectrum, calculated using SRIM 2012 [2], is given in Figure 1.

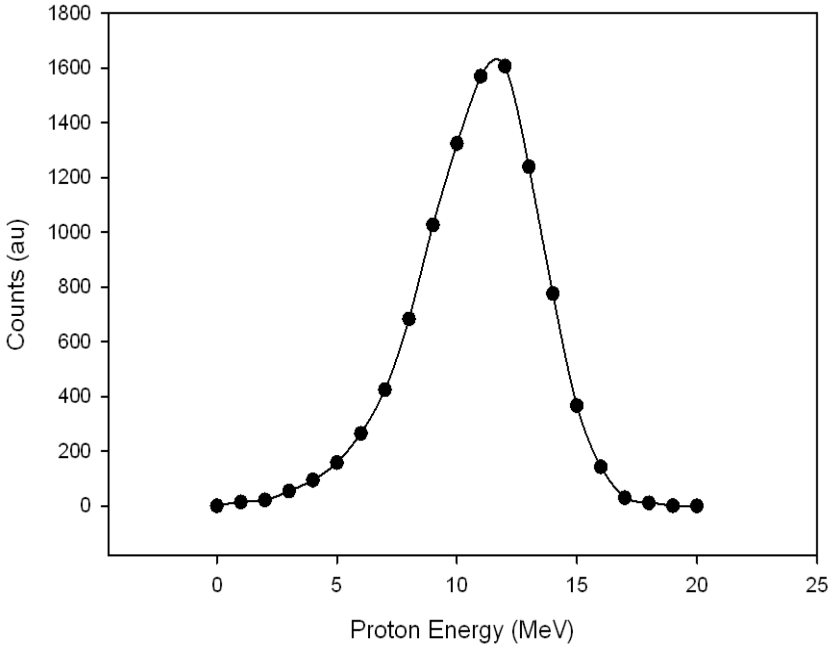

Figure 1 The calculated proton spectra with a mean energy of 10 MeV degraded from 74 MeV.

For low energy irradiations it is particularly important to understand the effects of any window materials, considering both the window attached to the device package and the window to any Dewar arrangement. An illustration of the effects of a borosilcate cover glass on incident proton energies is given in Figure 2. For alpha and electron irradiation it is likely that any window material should be removed completely during irradiation. The effect of window materials can be estimated using the SRIM code, for example.

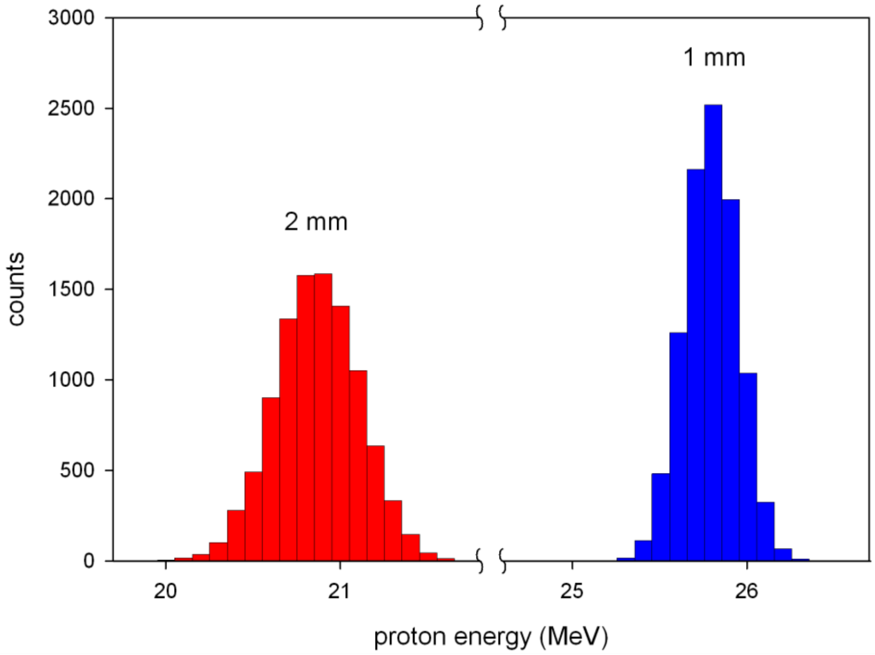

Figure 2 The proton spectra following transmission of a mono-energetic, 30 MeV, incident proton beam though two thicknesses of borosilicate glass.

3.2 Particle Flux

The proton flux is usually selected to ensure that the time required to reach a specified fluence is within acceptable practical limits and to minimise beam time, but is not too high so that dosimetry becomes problematic.

In practice proton irradiations for displacement damage testing are normally performed with fluxes in the range 10^7 – 10^8 p/cm^2/s. This, however, is very much higher than the flux experienced in the space environment. During steady state irradiation primary defects are introduced and reordering occurs continuously and short and long term thermal annealing occurs. If the rate of steady state irradiation and the primary defect introduction rate, is much lower than the short term annealing rate for introduced defects, then the damage produced after a given time will be relatively stable. In this situation, when irradiation is stopped the slow long term annealing process will be observed. If the rate of irradiation is of the same order as the annealing rate then the damage observed directly following the irradiation will be dependent on the particle flux. For room temperature irradiations there does not seem to be any evidence that this high flux usually used gives spurious results. However, the flux has be shown to affect the kinetics of defect generation [3] in silicon following 1.3 MeV proton irradiation at room temperature. For most of the radiation induced defects observed the introduction rate reduced significantly at fluxes very much greater than 10^9 p/cm^2/s. However, the introduction rate of a shallow defect, attributed to the vacancy oxygen complex, was flux dependent even at a flux of 10^7 p/cm^2/s, the lowest flux investigated. This may have implications for the CTI degradation of CCDs operating cold. However, the effect was less pronounced in the epitaxial material with relatively low oxygen content [4] usually used in the manufacture of CCDs.

At very high proton fluxes (>10^{10} p/cm^2/s) the temperature of the device under test could be increased significantly thus affecting the annealing rate.

3.3 Angle of Incidence

Most irradiations are undertaken with the irradiating beam normal to the surface of the device under test. Modelling work performed in [5] indicated that the mean damage energy loss rate (and thus the NIEL) was independent of the angle of incidence, but the variance was dependent on the sensitive volume geometry. A 40% difference in the variance was calculated for an 11 µm by 7 µm slab of silicon, 1µm thick, depending on whether the direction of irradiation was normal to the surface or parallel. The difference increased to a factor 4.4 for a 0.1 µm thick slab. This could have implications for the displacement damage induced dark signal distributions. However, this should not be of importance for most image sensor technologies currently used in space applications, where the depletion depths are significantly greater than these thicknesses.

3.4 Irradiation Temperature

Most irradiation campaigns are undertaken at room temperature. This appears to be reasonable if the mission performance is dominated by charge transfer degradation. For example, Hopkinson et al. [6] felt that irradiating at room temperature gave a good indication (between a factor 2 and 3.5) of the degradation that would be observed if irradiated cold, under the operating conditions of the GAIA mission. However, as discussed in Appendix A6.4, the device temperature affects the defect kinetics and the creation of stable defects following irradiation. It has been shown that annealing of hot pixels can occur in CCDs below room temperature. This implies that room temperature irradiations do not give a good estimate of on-orbit effects for cooled imagers, especially if the number of hot pixels is an important mission parameter. This has been seen in the in-orbit data from the CCDs used in the Hubble Space Telescope and has been particularly well illustrated by the work on low temperature alpha particle irradiations of silicon CCDs performed by Hopkinson et al. [7]. As another example, consider HgCdTe detectors with a normal operating temperature below 200K. The irradiation of these detectors at room temperature underestimates the degradation in dark signal that would be observed in operation, as a significant proportion of the dark signal will be annealed at temperatures above 200K, but will not anneal significantly at the operating temperature.

Ideally, therefore, irradiations should be undertaken at or near the expected operating temperature with measurements performed without changing the temperature or, at least, following typical changes of temperature expected during the mission. However, it is not always possible to perform irradiations at very cold temperatures due to logistical difficulties. For example, the activation of any cryostat arrangement by the irradiating beam will make handling and the transportation of the vacuum system a reasonable time after the irradiation problematic. This activation issue is reduced significantly if a low energy proton beam (for example <10 MeV) is used for the irradiations.

Activation of the cryostat and other components also requires careful consideration of the data acquisition details to ensure that, for example, enough frames are acquired for rejection of events due to signal generated from radioactive emission. This is particularly critical for in situ testing in a cryostat for multiple proton increments. In some cases the induced radioactivity has short lifetimes, and one can wait and take sequential sets of data. It is application dependent, but activation has to be carefully considered else a corrupted data set may be the result.

3.5 Bias During Irradiation

The initial defect concentrations produced by displacement damage are usually considered to be independent of bias applied during irradiation. Therefore displacement damage testing is usually undertaken unbiased. Unbiased irradiations tend to lead to a reduction in the effects of total ionising dose and therefore displacement damage effects can be isolated more easily. Comparison between the results obtained for devices biased and unbiased during irradiation confirmed that the increase in the dark current observed in InGaAs detectors used on the SPOT 4 satellite due to displacement damage does not depend on the bias applied [8]. A direct comparison between clocked und unbiased irradiations for silicon CCDs has been undertaken as part of this current contract [AD2]. No significant difference was observed for dark signal, DSNU, RTS and CTE degradation. However, for all parameters tested, the rate of room temperature anneal did depend on whether the device remained clocking or left unbiased. This implies that there will be a reduced degradation observed for very low dose rate, room temperature irradiations. More work is required to fully characterise and understand this bias dependent behaviour.

3.6 Beam Uniformity

Beam uniformity information should be available from the irradiation facility. The level of uniformity should be appropriate for the required testing. If the uniformity is marginal, for example if the device under test is particularly large in relation to the specified beam diameter, or if several devices are being irradiated at the same time, the beam should be characterised prior to irradiations being undertaken. There are several ways in which the uniformity can be determined. For example, radiochromic film or a scanning photodiode can be employed. Once the beam uniformity has been determined the device under test should be carefully aligned to the centre of the beam where the uniformity is likely to be optimum.

3.7 Exposure in Air or Vacuum

The choice of whether testing should be undertaken in a vacuum depends on the attenuation of the particle beam as it passes through air. This, in turn, is dependent on the particle type and energy. For reference, the projected range for protons and alpha particles in air is given in Figure 3.

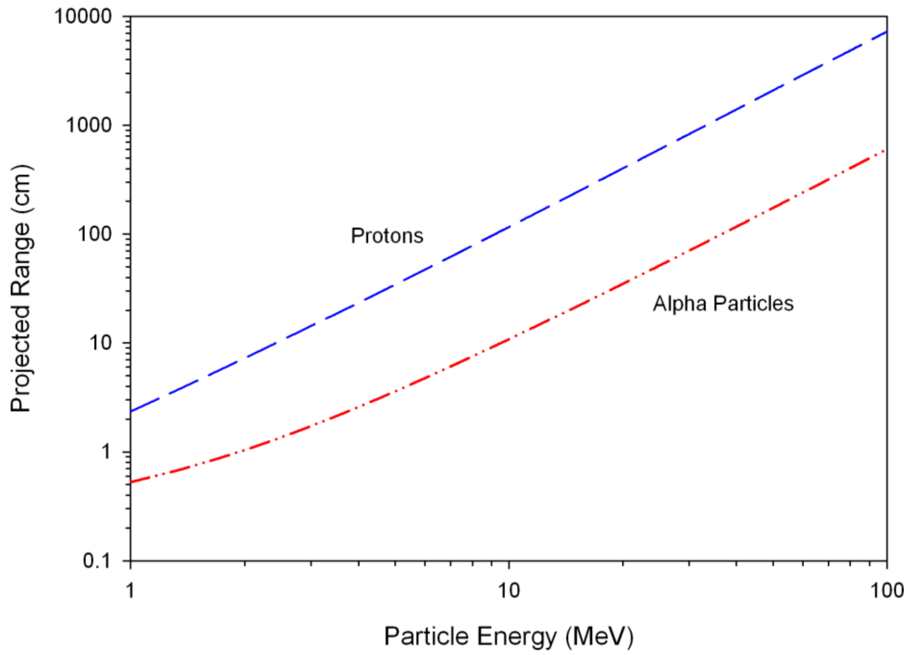

Figure 3 The range of protons and alpha particles in air at sea level

4 IRRADIATION SOURCES

Generally, irradiations need to be undertaken at facilities set up to generate the required particles. There are many irradiation facilities suitable for displacement damage assessment available throughout the world and a useful compendium of facilities has been drawn up and presented at RADECS 2011 [9]. In this section an overview of the general types of irradiation facilities are covered. For some studies, irradiation may be undertaken within the laboratory. Typical sources used for this type of activity are described in section 4.4.

4.1 Proton Sources

Most proton irradiation facilities supply protons through the use of Tandem Van de Graaff generators or particle accelerators such as cyclotrons or synchrotrons. Linear accelerators are also employed occasionally. Many are used for medical or industrial purposes and may not always be available for devices testing. It is certainly advisable to visit the facility prior to a radiation campaign to ensure it meets any specific requirements for, for example, accessibility.

Most Tandem Van de Graaff based facilities provide protons having an energy up to around 10 MeV. Examples include the Helios-3 facility of Synergy Health Ltd. (formerly Isotron Ltd.) in the UK and the SNICS source at CNA in Spain. Some facilities do offer higher energies, such as the SIRAD-INFN facility in Italy which provides protons up to 30 MeV. Generally the beam sizes tend to be a maximum of a few cm in diameter although the maximum irradiated area can be sometimes increased through the use of scanning techniques.

Cyclotrons tend to be employed when higher energies are required. Typically energies of up to a few tens of MeV are available from these facilities but some offer energies as high as 200 MeV. For example, the cyclotron at the Université Catholic de Louvain, Belgium, provides protons up to 62 MeV and low energy beam line at the Paul Scherrer Institut (PSI), Switzerland supplies energies up to 72 MeV. Beam diameters of 10-20 cm are typical. For very high energies synchrotron facilities are available for irradiation programs, such as the linear accelerator fed synchrotron at the Brookhaven National Laboratory, USA, which offers energies up to 2.5 GeV.

If proton energies are required below the maximum available, energy reduction is possible by either tuning the beam or through the use of degraders. Degraders are material plates, usually aluminum, placed between the beam and the device under test, the material and thickness being chosen to achieve the required energy. Although convenient, degraders should be considered with care as, although the mean energy will be reduced, straggling causes a broadening of the energy spectrum. This may result in a more complex analysis of the test results (see section 3.1 and Figure 1).

4.2 Neutron Sources

Neutrons for device testing can be provided by radionuclide sources, including neutrons from sources in a moderator, those produced by nuclear reactions with charged particles from accelerators and neutrons from research reactors.

The most commonly used spontaneous fission source is the radioactive isotope californium-252. This produces a spectrum of fission neutrons peaked at 1 MeV and extending out to ~13 MeV (Figure 4). Alpha reaction sources are also used, such as AmBe or AmLi.

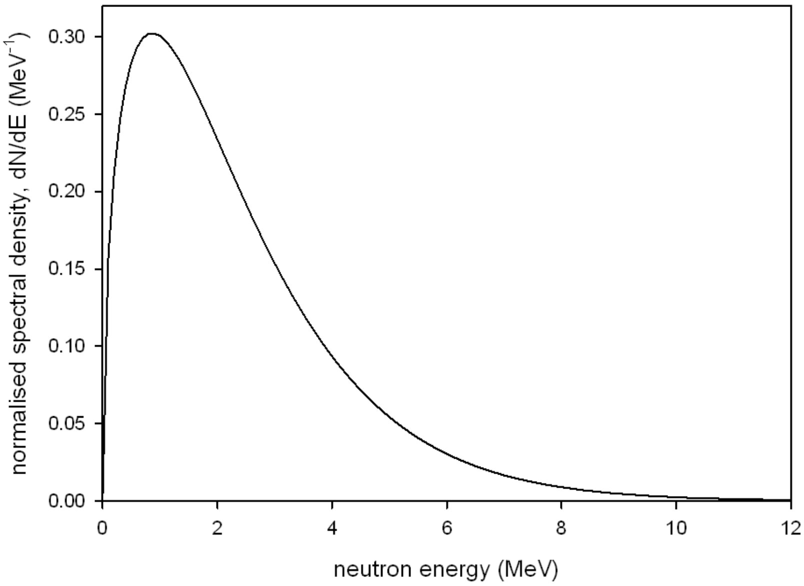

Figure 4 Spectra of the fission neutrons from Cf252 (after data provided in [10])

Mono-energetic neutrons can be provided by facilities that take advantage of the deuterium-tritium (14.1 MeV) or deuterium-deuterium (2.5 MeV) reaction through an accelerated ion beam hitting a metal hydride target, for example. The deuterium-tritium reaction provides an isotropic 14.1 MeV neutron source. Such facilities are available at, for example, the Atomic Weapons Establishment in the UK or the Fraunhofer Institute, Germany.

High energy neutrons are available from nuclear spallation facilities where a high energy proton beam, produced by a cyclotron or synchrotron, for example, impacts target material such as Tungsten. The neutron energy extends from thermal up to the energy of the incident proton beam. For example, the spallation source at the Svedberg Laboratory at Uppsala University, Sweden provides neutrons up to 180 MeV. The quasi-monoenergetic neutron (QMN) facility at the same laboratory produces neutrons from accelerated protons incident onto a ^{7}Li target. The resultant neutron spectrum is dominated by a high energy peak at an energy controllable between 17 MeV and 180 MeV.

4.3 Electron Beam Facilities

High energy electron beams can be provided by Van de Graaff generators or various linear accelerators. Maximum available energies range from a few MeV to a few tens of MeV. Most beam diameters are limited to a few centimetres but irradiation area can be increased by scanning of the beam. For example, the electron beam irradiation facility at the Japan Atomic Energy Agency Advanced Radiation Research Institute offers electrons up to 2 MeV over a scanned area of 5cm x 120cm. Electron beam irradiation can also be delivered from solid-state accelerators and so provide a DC beam, in contrast to LINACs. This affects the instantaneous dose rate which can be an issue. For these machines, however, the maximum energy available is around 5 MeV.

4.4 Laboratory Sources

The use of laboratory sources can be very convenient as they can, for example, be mounted inside the testing cryostat, enabling irradiation and testing at low temperatures without the need to bring the device up to room temperature. One of the difficulties in using a laboratory source is in the determination of the displacement damage dose deposited in the sensitive regions of the device under test due to the range of irradiating energies and the energy lost in intervening layers. An estimate may be made through conventional dosimetry methods, such as the measurement of generated currents, if the spectrum of the radiating particles is known. Particle counting techniques may be employed if the dose rate is very low.

A ^{90}Sr source has been used to study the effects of bulk damage on CTE in CCDs [11,12]. This convenient source produces betas from a ^{90}Sr to ^{90}Y transition and a ^{90}Y to ^{90}Zr transition having a spectrum with an end point energy of 2.3 MeV. The energy spectrum [13] is shown in Figure 5. A 20 mCi source mounted at reasonable distances from the device is sufficient for displacement damage to be observed following practical irradiation times.

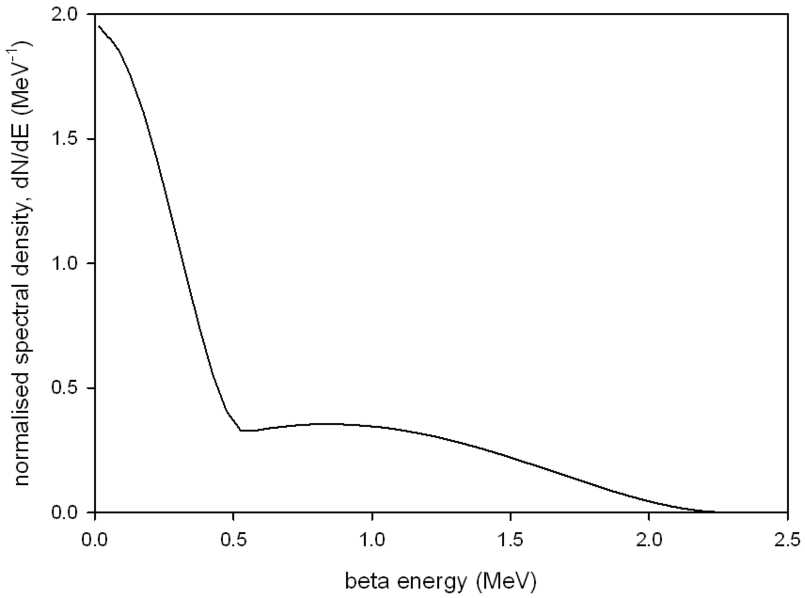

Figure 5 The differential energy spectrum of the beta particles from a ^{90}Sr source.

The use of an ^{241}Am alpha source to simulate the space environment has been discussed in [14] and used successfully for low temperature studies in [15]. This is an artificially produced source having a half-life of 462 years. The generated alpha particles are reasonably monoenergetic, having an energy of 5.5 MeV. As the alphas are highly ionising significant energy will be lost as they pass through the material holding the source and any window foils, for example. It was estimated in the previous studies that the mean alpha particle energy incident on the device under test was around 4.6 MeV. A ^{210}Po Alpha source has been used for dark signal studies [16]. This produces alpha particles having an energy of 5.3 MeV, very similar to those from ^{241}Am. It is probably not as practical for general use as its half life is only 138 days.

5 DOSIMETRY

ASTM Standards exist for the dosimetry of neutron beams for testing electronics for displacement damage but an equivalent set of standards has not yet been developed for proton beams. However, standard practice for dosimetry of proton beams has been discussed by McMahan et al. [17] and this may, in future, be adopted by ASTM. McMahan et al. recommend that the proton fluence should be determined to better than 5%. The proton beam should be monoenergetic or near monoenergetic ($\Delta E/E < 5\%$) and the energy should be known to < 2-5% depending on the application. They also recommend that beam flux density should be uniform to within 5-10% across the size of the device under test (DUT). In practice the dosimetry may sometimes be to only 10% accuracy. Though not ideal, this should be acceptable for many applications.

In the following sections a brief overview of dosimetry techniques is given.

5.1 Faraday Cup

A description of the use of the Faraday cup has been given by Cascio and Gottschalk [18]. A Faraday cup has a shielded, insulated target block thick enough to stop the incident protons. The charge deposited in the block is measured (e.g. with an electrometer) and is proportional to the number of stopped protons. Electrostatic and magnetic fields are often used to suppress the current from external secondary electrons or to prevent secondary electrons generated within the cup from escaping. Faraday cups do not provide absolute real-time monitoring; they are moved in and out of the beam or are placed in a separate area to provide measurements only when needed for calibration of other detectors.

5.2 Scintillators

A scintillator is a material which, when irradiated, converts a fraction of the interacting particle energy into light. The light output is proportional to the ionising energy lost by the incident particle. The generated photons can be detected by a photomultiplier or avalanche photodiodes, for example. These detectors can be used for real time monitoring of the flux and various arrangements can be employed.

5.3 Diffused Junction and Surface Barrier Diodes

The current generated in the diode by the incident ions is proportional to the ionising energy deposited. This can then be related to the ion flux. Semiconductor surface barrier diodes have also been used to measure fluxes of neutrons. In this case it is the current generated by ionising products of the neutron interaction that is detected [19].

5.4 Secondary Electron Monitors

If an irradiating beam passes through thin metal films such as aluminised Mylar secondary electrons will be generated. If the films are connected to a picoammeter the resultant current is proportional to the number of ions passing through the foil. This simple arrangement can be adapted by appropriately biasing and segmenting the foils to enable the determination of the beam uniformity and focus.

5.5 Radiochromic Films

Radiochromic films are frequently available for on-demand testing of a beam’s uniformity in a purely qualitative manner. The film is exposed to a dose known not to saturate the film. The film is then read by any number of means, but the most popular method is to scan the film with a simple flatbed scanner into a gray scale (0-255) image, and process it with a commercially available software package.

5.6 ESA SEU Monitor

The ESA SEU monitor [20] was primarily designed as a reference for evaluating beams for single event upset testing. However, as the SEU cross sections for the detector element are known over a wide range of ion LETs and neutron and proton energies, the SEU monitor could also be used as a cross check to monitor the ion fluence for displacement damage studies.

5.7 2-D Imagers

2-d imagers themselves can be used to count the number of incident particles if the particle flux is sufficiently low. This technique has been used to assess the flux of alpha particles, for example.

6 IRRADIATION PLANNING AND PROCEDURES

6.1 Preparation of Test Plan

It is usual to try to standardise test procedures as far as possible. That way, test planning is simpler and results from different tests can be compared easily. Standard test methods exist for total dose and single event effects testing and some ASTM guidelines relate to neutron testing [21]. However, standard methods do not yet exist for displacement damage testing. Therefore a test programme for displacement damage has to be tailored to individual requirements. It is suggested that the following items be included within the test plan.

- Details of the Test Facility
- Test particle (electrons, protons, alphas or neutrons)
- Test energy, or energies
- Fluence intervals
- Irradiating particle flux
- Irradiation temperature
- Uniformity requirement
- Number of devices to be tested
    - including batch numbers and wafer lots if applicable.
- Bias conditions
    - whether a devices is unbiased with all pins connected, DC biased or clocked
- Annealing tests to be performed
- Time following irradiation when tests are to be performed
- Parameters to be measured and related test methods
    - The parameters to be tested must include the parameters that are important for successful operation of the mission, including those expected to change following the irradiation. An important point to note is that the tests will only see what they are looking for. If a parameter or effect is not known about (or not thought important) and is not tested for then it will not be seen and will go unnoticed until it occurs during operation. This is a particularly difficult problem for complex devices that may have unusual failure modes.

As well as ensuring the testing is undertaken as expected, including these items will help reliable cross referencing between the test results and those available from other campaigns.

If TID testing is to be undertaken at the same time as the displacement damage testing then elements within RD1 and RD2 should be considered also.

It should be noted that a “design of experiments” approach has been taken to develop a test plan to establish a predicted end of life performance for phototransistor arrays [22]. This approach may have some benefit in the evaluation phase of a programme, especially for devices where the inter-relationships between TID and displacement damage is complicated and not additive, for example in bipolar transistors or optocouplers. However, for most image sensors it appears that degradation due to TID is independent of the degradation from displacement damage and a simpler approach is often more appropriate.

6.2 Number of Devices

The recommendation of the number of devices to be tested is one of the more difficult issues with displacement damage testing as it relates to the expected level of device-to-device and lot-to-lot variations. To a certain extent, the number will depend on the experience in dealing with the manufacturer and the quality and type of relevant radiation data provided. Little work has been done in this area since devices are expensive and usually only small numbers are available.

Whether to undertake a LAT programme for displacement damage effects is ultimately a project decision based on an assessment of the risks and the project approach to risk mitigation. Many programmes will want to follow a full LAT approach. However, the issue of device-to-device variability is linked to the nature of the defects involved in the degradation. For intrinsic defects (due to vacancies and interstitials, or their aggregates) there is likely to be little variation since their concentration will be fundamental to the interaction of the radiation with the semiconductor material. For defects that are associated with dopants (e.g. the phosphorous-vacancy complex, the S-E centre) there should again be little variability since the dopant levels should be closely controlled. However defects associated with impurities (e.g. carbon or oxygen) will vary with impurity concentration, which may vary with wafer lot. Hence it is important to identify the nature of the dominant defects involved. The most important issue concerns dark current in CCD and CMOS imagers, where the defect type has not been positively identified. However, the fact that a universal damage constant appears to describe the dark signal generation in silicon devices points to the fact that the main defect responsible is likely to be intrinsic in nature. For CTE degradation the situation is not as clear cut. In operating regimes where the divacancy or the Si-E centre dominates there is likely to be little variation between devices of the same type and electrical characteristics. However, if the operating conditions are such that the low levels of "unknown" defects dominate then considerable variation between lots may be expected. Suggested wafer lot testing requirements for silicon CCDs is given in Table 1. Similar suggestions for other silicon imagers can be made also. However, insufficient data for IR imagers is available to make a recommendation not to do lot to lot testing of these devices.

Table 1 Suggested wafer Lot to lot displacement damage testing requirements for silicon CCDs

Parameter	Conditions	Lot testing necessary	Comments
Mean Dark Signal	Assumes no dark signal from Si/SiO_2 interfaces	No	Si/SiO_2 interfaces not depleted
Dark signal distributions (DSNU)	Assumes no dark signal from Si/SiO_2 interfaces	No	Si/SiO_2 interfaces not depleted
RTS	Assumes no RTS from SiO_2 or Si/SiO_2 interfaces	No	Si/SiO_2 interfaces not depleted
CTE	$T>\sim-60^oC$	No	Assuming that the operating conditions are such that the Si-E centre or divacancy dominates the degradation.
CTE	$T<\sim-60^oC$	Yes	Assuming that the operating conditions are such that the Si-E centre or divacancy does not dominate the degradation.

When evaluating the performance of large area imagers, a single device can be masked (shielded) during irradiation so as to produce several fluence regions. This will obviously reduce the number of devices required for an evaluation programme. For example 10 MeV protons can be masked using 1.5 mm thick aluminium plates. At higher energies thicker (and/or denser) shields are needed as shown in Figure 6. Shielding calculations can be conveniently performed using SRIM. Care must be taken when irradiating with high energy protons as neutrons generated within the shielding material may cause additional displacement damage dose to be deposited, even if the basic shielding calculations show that shielding is sufficient.

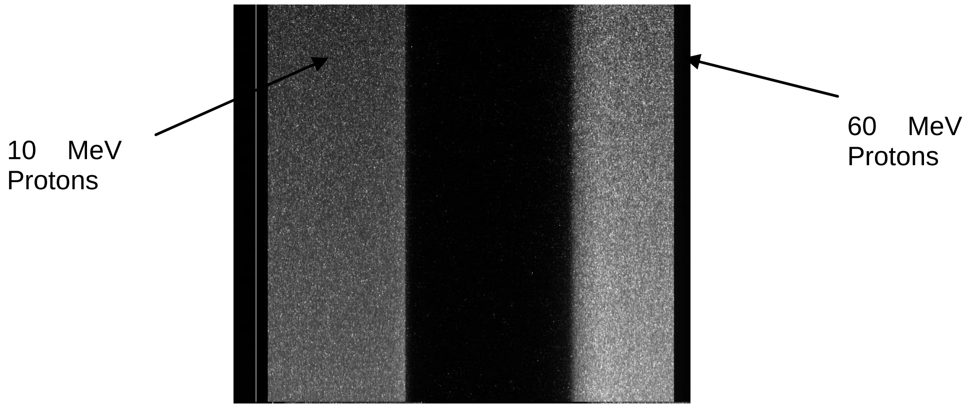

Figure 6 Dark image for a CCD masked to give regions irradiated by 10 and 60 MeV protons. There is some non-uniformity across the region exposed to 60 MeV protons due to the scattering off the thick shielding (8 mm steel) required at these high energies.

6.3 Radiation Design Margin

The radiation design margin (RDM) is factor difference between the specification of the radiation environment for a device and the radiation level at which the performance becomes unacceptable. The margin policy in a project normally requires a minimum factor that is acceptable to account for uncertainties in the radiation effects evaluation process, including uncertainties in the definition of the environment and extrapolation of the tested device performance to operational conditions. The design environment specification is part of the product requirements, which should include qualification margins. The RDM is defined as:

$$RDM = \frac{D_{fail}}{D_{env}}$$

where D_{fail} is the worst case dose (for the devices sampled) resulting in the failure of the performance parameter, and D_{env} is the specified environmental dose. In the case of displacement damage these doses should relate to the non-ionising dose.

Reference [23] outlines the elements that contribute to the uncertainties leading to margins and provide guidance on deriving a particular margin value. Contributions to the margin include

- Uncertainty in the knowledge of the actual environment (e.g. uncertainty in the models)
- Uncertainty in predicting effects parameters and extrapolating from test data
- Uncertainty in the effects of shielding or even the shielding definition at the time of test
- Systematic and statistical uncertainties in the testing
- Procurement processes (e.g. procurement from a single wafer lot)
- Project management decisions

Typical values, depending on the criticality of a parameter, would be an RDM of 2 to 5 but is ultimately a project management decision. CNES, for example, usually utilise an RDM of 1.2 if the devices being tested belong to the FM batch and an RDM of 2 otherwise.

6.4 Organisation Aspects

6.4.1 Booking the Irradiation Facility

The method for booking the facility varies from place to place. Advice should be obtained directly from the facility but booking as far in advance of the intended test date is strongly advised. Consideration should be taken of any shut down period for maintenance or upgrade.

6.4.2 Device Mounting

Jigging will be required to present the device to the beam or other radiation source. The mechanical interfaces will be dependent on the radiation facility from which detailed requirements must be obtained.

For high energy beams, for example a proton beam with energy greater than about 10 MeV, induced radioactivity must be considered. The half-life of the induced activity depends on the type of material. Materials composed of low Z elements, such as plexiglass, generally have short half-lives in the order of minutes, whereas high Z materials, such as Au, will have much longer half-lives, extending into days or even weeks. The use of steel screws is particularly problematic as the half-life here runs into hundreds of days. Therefore any mechanical arrangement exposed to the beam, including cryostat arrangements and various fixtures, should be manufactured from low Z materials to minimise logistical complications.

6.4.3 Protection of Devices and Support Equipment

Irradiation of sensitive equipment by the irradiating beam or the scattered radiation present in the chamber during testing must be considered, especially if the equipment is located close to the radiation source. Any equipment required to be in the radiation chamber should be placed as far from the source as possible and suitably shielded. For proton irradiations shielding against the neutron background may be necessary but is unlikely to be a major issue.

6.4.4 Remote Monitoring

In proton and neutron facilities personnel cannot be present in the irradiation room whilst devices are being irradiated. Therefore, devices must be controlled remotely using long cables passing through to a control room.

6.4.5 Shipping

All goods that are exported temporarily or permanently to a radiation facility across national boundaries must be cleared through customs. Some facilities provide assistance and advice on the generation or the appropriate documentation, for example. Complications arise should the shipment contain radioactive material so irradiated material is usually held at the facility until the induced radioactivity falls to appropriate levels.

6.5 Radiation Safety

Radiation safety is of utmost importance due to the health risks associated with exposure to the particle beam during exposure and any additional radioactivity present after irradiation has completed. Some facilities require a medical be undertaken before access to the facility is granted. In most cases a radiation badge will be issued to monitor exposure levels.

6.5.1 Safety Interlocks

Safety interlocks are designed to ensure source or beam exposure cannot occur if there are personnel present.

6.5.2 Device/Materials Activation

A significant source of hazardous radiation originates from the material activated by the primary radiation source. This radiation has a half-life that depends on the type of material. Elements with a low atomic number, such as aluminium, tend to have a short half-life in the order of minutes. Therefore any hazard will reduce rapidly and the device under test can be removed from the facility promptly. Materials having a high atomic number, such as gold have much longer half-lives, in the order of days. Therefore the devices must be left at the facility following irradiation until the activation reduces to safe levels. Facility personnel will be able to monitor the samples and advise when they are safe to be transported. Because of the logistical difficulties the induced activity presents, the use of high atomic number metals in test fixtures should be avoided.

6.5.3 Food and Drink

Food is not allowed in any areas where there is a possibility of radiation contamination from radioactive dust, for example. Hands should also be washed after being in the radiation chamber.

7 TEST MEASUREMENTS

This section provides an overview of various test methods that can be applied to the evaluation of displacement damage to image sensors. A useful guide to various methods and the relation to system performance can be found in [24].

7.1 Output Calibration

To make many quantitative measurements the signal acquired from the device has to be related to the number of electrons generated within the array. This calibration is necessary to enable comparison of the results with those obtained by other institutions and published within the literature. It may be also necessary to enable the modelling of device and system performance.

7.1.1 Mean Variance

There are several methods to achieve calibration, one of the most universal being the use of the so called mean variance method (also known as the photon transfer method). This has been covered in [25] and many practical issues discussed in [26]. In essence the principle is very simple, as follows.

The mean signal out of the device is given by

$$S_{out} = K \times N + O$$

where *N* is the number of electrons generated by the optical illumination, *K* is the conversion factor and *O* is an offset. The noise variance out of the device is given by

$$\sigma_{out}^2 = K^2 \sigma_N^2 + \sigma_R^2$$

where σ_N is the noise on the generated electrons and σ_R is the readout noise and other noise sources. As the noise on the generated signal electrons obeys Poisson statistics we have

$$\sigma_N^2 = N = \frac{S_{out} - O}{K}$$

giving

$$\sigma_{out}^2 = K(S_{out} - O) + \sigma_R^2 .$$

If the output noise variance is measured as a function of output signal a plot of noise variance versus mean output signal should provide a linear fit with a gradient giving the conversion factor, *K*. This is a convenient method for calibrating the device although complications arise if, for example, the device has significantly nonlinear behaviour [25] or if it is a CCD with poor charge transfer efficiency.

The variance versus mean signal plot can be generated for each output of a CCD by acquiring flat field images over a range of signal levels and calculating the signal means and variances for each image. However, this requires very good signal uniformity. Alternatively the mean and variances from individual pixels can be calculated by taking many images at each illumination level, and calculating the mean and variance for each pixel. This removes the uniformity requirement but does need the illumination to be stable whilst frames are captured. This method also enables the responsivity of individual pixels of a CMOS sensor, or those of a Hybrid sensor, to be measured.

A convenient way to generate a mean variance plot for a CCD is to illuminate the device with a test chart whilst continuously reading it out. For a full frame device the sequence of transferring a row to the readout register and reading it out is continuously repeated. A similar sequence is used for a frame transfer device with the image and store sections clocked together. The resultant image will be smeared in the parallel transfer direction. Image acquisition commences once a minimum of the number of rows in the device have been readout following illumination, the image used for analysis being made up of over-scan rows. The number of over-scan rows should be sufficient to calculate the mean and variance in the signal from each column. The use of a test chart having a checkerboard pattern, as illustrated in Figure 7, results in an image for analysis shown in Figure 8. Any test chart can be used but a checkerboard pattern gives a wide range of signal levels. For each column the mean signal and variance can be calculated and once plotted the value of *K* can be determined. A typical variance versus mean plot using this technique is given in Figure 9.

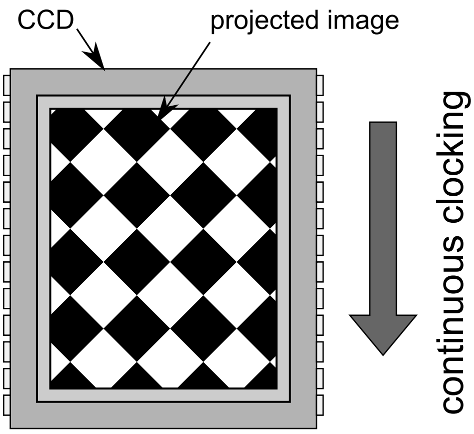

Figure 7 The projected test chart used for mean variance calculation for a CCD

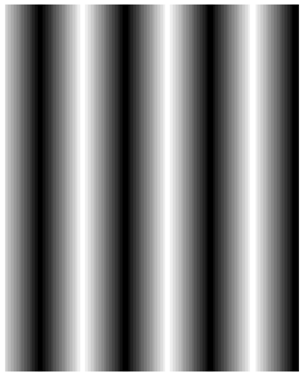

Figure 8 Image acquired for mean variance method using continuous clocking and exposure to the test chart of Figure 7.

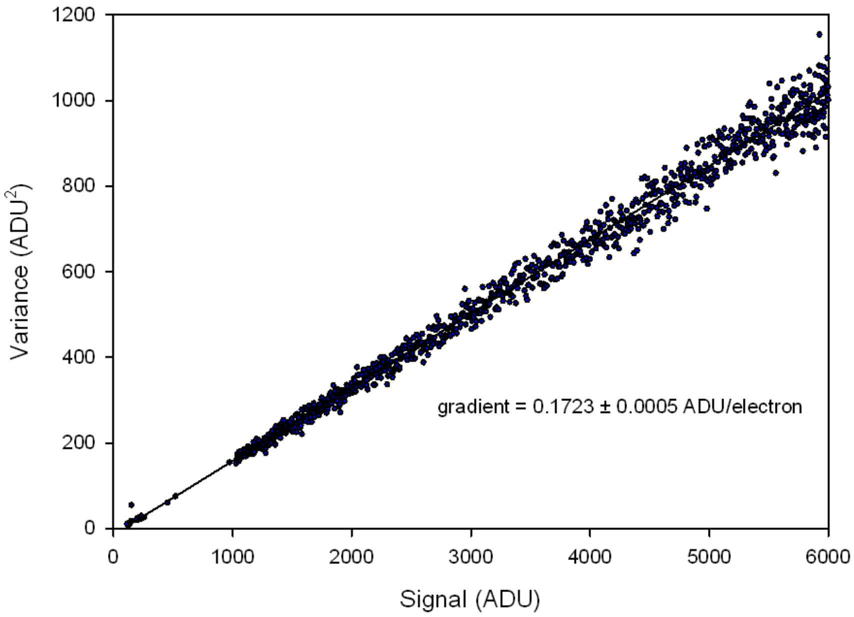

Figure 9 Variance versus mean signal in a column plot for the calculation of system response

7.1.2 Reset Current

If the user has access to the reset lines of the device an alternative method of calibration is to monitor both the current flowing down the reset lines and the output signal whilst the device is being operated and illuminated. If the device is a uniformly illuminated CCD, which is being continuously clocked, the system response is given by

$$R(\text{V/electron}) = f(\text{Hz}) \times \frac{V(\text{Volts})}{I(\text{Amps})} \times q(\text{Coulombs}) \times \phi$$

where f is the readout frequency, V is the mean output signal in each pixel, I is the mean current flowing down the reset line, q is the electronic charge (1.602 x 10^{-19} C) and ϕ the fraction of a line containing signal to allow for over-scan pixels, for example. For a digitised signal V is replaced by the digital output in ADU resulting in a system response in terms of ADU/electron).

As the generated signals tend to be small, the measured currents can be affected by various leakage currents. However, the problem can be eliminated by measuring the change in output signal, ΔV, and drain current, ΔI, for a change in illumination level, and using

$$R(\text{V/electron}) = f(\text{Hz}) \times \frac{\Delta V(\text{Volts})}{\Delta I(\text{Amps})} \times q(\text{Coulombs}) \times \phi \,.$$

7.1.3 X-Ray Method

When x-rays interact with a semiconductor material via the photoelectric effect, electron hole pairs will be generated. In general it takes an average energy around three times that of the band gap to create one electron hole pair in a semiconductor [27]. The mean number of electron hole pairs generated per interacting x-ray is simply

$$N = \frac{E_{xray}}{E_{eh}}$$

where E_{xray} is the x-ray energy and E_{eh} is the mean energy to generate an electron hole pair.

In silicon, at x-ray energies greater than ~1 keV, 3.7 eV is required on average for each electron hole pair at a temperature of 183K [28]. Thus, if the output signal is measured for a device exposed to x-rays having a known energy, the system response can be calculated. The x-ray source most often used for device testing is ^{55}Fe for which the dominant x-rays are from the Mn K_α transition having an x-ray energy of 5.899 keV. In this case, on average, an interacting x-ray will generate 1600 electrons at -90 ^{0}C. (For a discussion on the signal generated by x-rays in silicon and the temperature dependence see [29].) If the x-ray interacts within a field free region of the device, these signal electrons diffuse to surrounding pixels. However, if the interaction is within the depletion region all of the signal electrons can be collected within a single pixel. A typical resultant histogram of the signal generated in a CCD is shown in Figure 10. The position of the peak corresponds to the mean signal generated by the Mn K_α x-rays and therefore this can be used to calibrate the system.

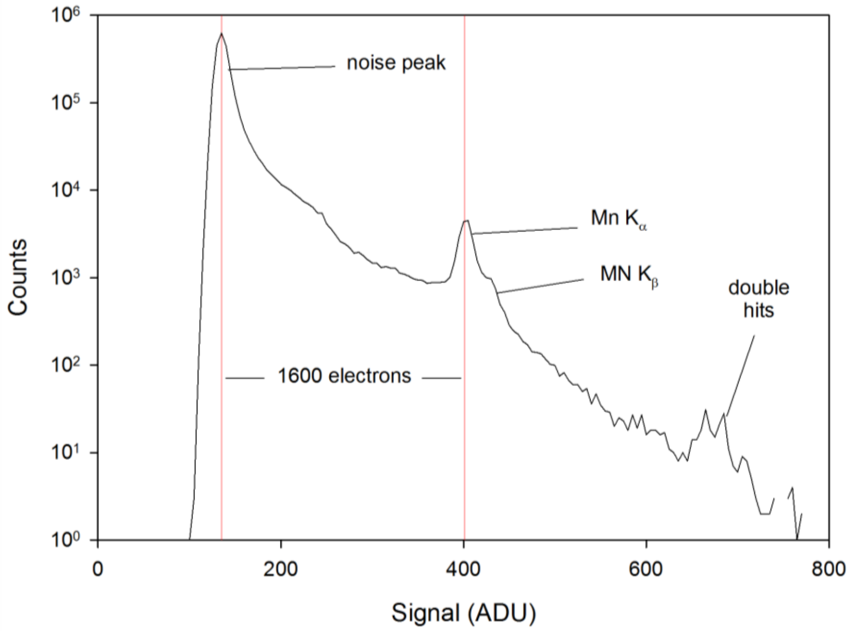

Figure 10 ^{55}Fe x-ray spectra obtained at -70 °C, from a CCD having a readout noise of ~25 electrons.

If the device under test has a sealed window, or the x-ray source has to be mounted outside a dewar, use of ^{55}Fe can be problematic as the x-rays can be completely absorbed in the window material. An alternative practical source yielding higher x-ray energies is ^{109}Cd. The dominant x-ray stems from the Ag $K_{\alpha 1}$ transition providing an x-ray energy of 22.2 keV [30]. This is sufficient for useful transmission through most practical window materials and, when interacting within silicon, a mean signal of 6000 electrons is generated.

The use of the x-ray technique is most often used for calibrating silicon devices. However, some work has been published on its possible use in calibrating HgCdTe image sensors [31]. For devices having a cut-off wavelength of 1.7 µm on average around 3.2 eV was found to be required to generate an electron hole pair.

7.2 Dark Signal

The mean dark signal is defined as the rate of generation of signal when the imager is not exposed to illumination. The usual units employed when quoting dark signal are electrons/pixel/second or nA/cm^2. The conversion between the dark signal units must be done with care and it is important to note what area has been used in the conversion. For example, is the entire pixel area used or has the un-depleted areas of the column isolation regions been excluded?

Due to the temperature sensitivity the temperature needs to be stable during the measurement and measured to an accuracy, preferably, better than +/- 0.5 °C. As the dark signal is dependent exponentially on temperature, the temperature should be measured as close as possible to the device under test to reduce, as much as possible, temperature differences between the temperature sensor and the device itself. Measuring the dark signal as a function of temperature can be a useful diagnostic tool as this will give some indication as to the origins of the degradation. It can be useful, also, to enable extrapolation to the mission operating temperature. However, care must be taken with this approach as different dark signal components may dominate at temperatures much lower than the measured temperature range and extrapolation may give an underestimate of the dark signal at the mission temperature.

The dark signal will often depend on the biasing applied to the device. This could be due to field enhancement effects but more often the bias dependence is due to a change in dark signal components. For example, the dark signal due to displacement damage is proportional to the bias dependent depletion volume. Also, in CCDs for example, surface components of dark signal can be suppressed due to surface inversion or accumulation. To measure the degradation expected during a mission, it is necessary to measure the dark signal under as close to the mission operating conditions as possible and in any case, when the dark signal is quoted, it is necessary to state the bias conditions under which the measurements were taken.

Long integration times may be required if the dark signal is being measured with the device particularly cold. In this case care must be taken that the results are not corrupted by low levels of light leakage within the system or even light generated within the image sensor itself. For example, active loads used within a source follower may emit a low photon flux. This problem can identified if the measured signal has only limited or no temperature dependence. If the photon source is the device itself it may be reduced or eliminated by lowering the bias on output amplifier circuitry during integration. However this may not always be a practical solution.

There are also particular issues when testing infrared imagers at low operating temperatures as it can be difficult to provide a thermal shield sufficient to remove all surrounding thermal leakage that would be detected as signal. In some cases double or even triple shielding may be required. Contamination of the dark signal image can also occur through light generated from components within the ROIC.

7.3 Dark Signal Non-Uniformity (DSNU) and Defective Pixels

7.3.1 Dark Signal Distributions

The dark signal may not be uniform over the device area. This global non-uniformity may be due to how the device is operated, for example a frame transfer device CCD may show a linear ramp in the dark signal due to the dark signal collected during the readout of the storage area. A global non-uniformity may also be indicative of non-uniform irradiation so the dark signal “images” can be useful tool to check the irradiation process.

On a more microscopic scale the dark signal generation rate will not be constant from pixel to pixel. There may be charge injection from defective pixels but, more often, the pixel to pixel variation arises from the statistical distribution of the displacement damage and the creation of generation centres. The definition of a defective pixel is often mission specific and a pixel is counted as being defective when the dark signal generation rate is above a certain value. Obtaining a histogram of the dark signal values is useful for determining whether the defective pixels form part of the expected distribution or whether they lie outside the distribution significantly.

7.3.2 Random Telegraph Signals

To count the number of pixels demonstrating RTS behaviour many dark signal frames need to be collected over a period of time. The time period should be chosen such that the RTS pixels having a time constant of importance to the mission or the measurement can be detected. Care must be taken to ensure that the device temperature remains constant over the time of the measurement, which could extend over several days.

Counting the number of RTS pixels can be achieved by simply detecting whether the dark signal within each pixel changes by more than a certain value, the threshold being chosen to be sufficiently high such that false detection is minimised. It is often useful to review the image data by eye to ensure that the detected pixels do, in fact switch between generation rates. A more sophisticated approach to the detection of RTS pixels has been described by Goiffon et al. [32] which involves the detection of the edge of the transition as shown in Figure 11. This enables a robust and detailed characterisation of the RTS defects even when the RTS behaviour is multilevel in nature.

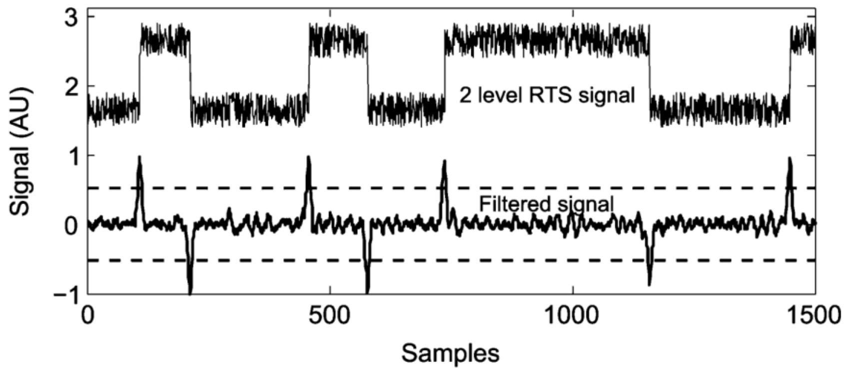

Figure 11 Illustration of the RTS edge detection technique [32] used on a simple 2-level RTS pixel.

7.4 Charge Transfer Efficiency

There are several basic methods for measuring the charge transfer efficiency (CTE) and variations within each method. Each method can result in a different answer as CTE is a complex function of the temperature, clock timings, signal size, and the distribution of signal within an image (see Appendix A6.3.4). For example, the CTE measured for large signals with signal present in most pixels in an image, will yield a much lower figure than from small signal packets in an image of a scene containing mostly empty pixels. Some methods have been compared by Waczynski et al. [33] for assessing CCDs used in the Hubble Space Telescope.

If the aim of the CTE measurement is to establish end of life performance then the device should be run under as close to the expected operating conditions as possible (including clock timings and temperature). A single CTE figure cannot be used to describe the degradation of even the simplest of practical images. Therefore a scene, typical of that of the mission, should be imaged by the device and assessed for imaging performance, for example, centroiding accuracy in the case of star trackers. However, obtaining a figure for CTE can be useful for detailed investigation into the physics involved in the degradation, for comparing performance of different technologies and for performing lot acceptance tests for example. The most widely used test methods are described below. If employed for lot acceptance tests, the method should represent as close to the expected signal levels and mission image characteristics as possible. However, this will not always be possible as the structures and light shielding of the device will make some methods impractical.

7.4.1 Periodic Pulse Technique

Some CCDs have dedicated structures to enable the injection of a known amount of charge into the image section or readout registers. This enables a flexible method for measuring the CTE, known as the periodic pulse technique, to be employed. The periodic pulse technique has been described by Mohsen and Tompsett [34] and by Collet [35]. A group of several consecutive signal packets, of equal size, are injected into the CCD and the output of the device monitored. The CTE can be obtained by measuring the signal size of the first, A, and last, B, charge packets in the group at the output. Assuming that all the traps causing a degraded CTE have been filled by the previous charge packets, the size of the last packet gives the size of the first packet in the group before any transfers have taken place. The charge transfer inefficiency, defined as the fraction of charge lost when a signal packet is transferred from one pixel to the next, is equal to 1-CTE and can be calculated from

$CTI = 1 - (A/B)^{1/N} \approx (B-A)/(NB)$ if the CTI is small.

Here N is the total number of pixels through which the charge has had to transfer to get to the output.

This method does rely on the ability to inject signal into the device reliably and with low noise.

7.4.2 X-ray Stacked Line Traces

When an X-ray interacts with the CCD it generates signal electrons, the number being dependent on the energy deposited. The x-rays from ^{55}Fe, for example, produce a characteristic spectrum, peaked at a signal size of 1600 electrons at a temperature of -70^{0}C, the peak originating from the 5.899 keV Mn k$_\alpha$ x-rays (see Figure 10). A mean signal level of 6070 electrons is generated by the 22.163 keV x-rays from ^{109}Cd. Sources providing x-rays with a significantly higher energy are not particularly useful due to the relative transparency of the active silicon layers and other techniques are generally used where larger signals are to be investigated.

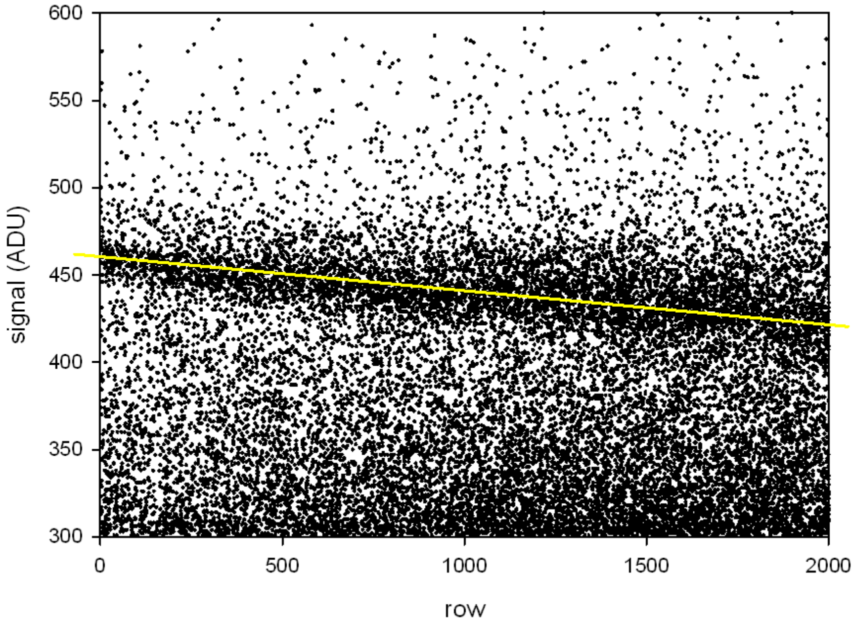

Figure 12 ^{55}Fe stacked line trace measured at -90^{o}C following a 10 MeV proton fluence of 6x10^9 p/cm^2.

Noting the signal lost from the spectral peak as a function of number of transfers, the charge transfer efficiency in both the parallel and serial transfer directions can be calculated. This is most readily measured through the use of the stacked line trace. A typical stacked line trace used to calculate the CTI in the parallel transfer direction is shown in Figure 12. Here the signal from each pixel is plotted as a function of row number. A linear fit is made to the points within the signal from the main spectral peak. The CTI is calculated from the gradient of the fit divided by the intercept minus the mean signal in the noise peak. Similarly the serial CTI can be calculated using the same x-ray image but plotting the signal in each pixel as a function of row position.

This method is only reliable if a good fit to the spectral peak can be achieved. For very small pixel devices, or devices with a large active thickness, it may be rare to see the entire signal from a single x-ray interaction appearing within one pixel. In these cases split events may dominate and the spectra will be ill-defined. Here event reconstruction may be useful but this complicates the interpretation of the CTE measurement.

Appendix A6.3.4 shows that the CTE is a function of time between charge packets passing through the same point in an array. It is clear that the CTE measured by the x-ray technique will be a function of x-ray hit rate, and thus source activity and integration time. Therefore the X-ray hit density must be specified when quoting CTE measured using this method.

7.4.3 Extended Pixel Edge Response

The extended pixel edge response (EPER) technique involves uniformly injecting signal into the CCD, ether electrically, or more usually optically, to produce a uniform image. The image is then read out but extra clock cycles are applied so as to measure the charge deferred to trailing or over-scan pixels due to the finite CTI, either in the parallel or serial transfer direction. This method has been described by Janesick et al. [36]. The CTI is calculated by summing the signal in a defined number of over-scan pixels and dividing this by the number of transfers and the signal in the illuminated pixels.

There may be some practical difficulties with this method, for example, the alignment of the light shield applied to the device, or signal diffusing into the pixels at the edge of the array from the periphery of the device, may mean that the signal in the final illuminated real pixel to be read out may not be representative of the flat field exposure. This may affect signal emitted into the over-scan pixels. It is also important to ensure that that all of the deferred charge is measured to avoid under estimating the actual CTE. This can be difficult where the emission time constants are long and the small signals emitted may be obscured by noise. However, if the summation of the differed charge is limited to a defined number of over-scan pixels, X, then it has been noted that the calculated CTE will be equivalent to the value that would have been obtained from isolated charge packets with a spacing equivalent to X pixels [37].

An important practical advantage of the EPER technique is that it requires no special equipment, only the provision of flat field illumination. Therefore it can be employed to monitor the CTE during a mission. It can also be used to measure the CTE over a wide range of signal levels and CTE values. However care must be taken to minimise system noise which will dominate the measurement uncertainties at small signals.

7.4.4 First Pixel Edge Response

The first pixel edge response (FPER), sometimes referred to as the first pixel response (FPR), technique is similar to EPER [38], but the charge missing from the leading edge of a flat field image is measured instead of charge in the trailing pixels. Usually, measuring the parallel CTE using FPER requires a frame transfer device with two areas split and independently clocked. For serial CTE measurement the readout register needs to be spit and independently clocked. To make a parallel CTE measurement using FPER, the CCD is exposed to a flat field illumination and then the storage region is readout. Then the image region is read out through the storage region. The first lines read through the empty storage array lose charge to the radiation induced traps. The total charge lost is measured for a given number of pixel transfers. This, divided by the number of transfers multiplied by the mean signal level gives the CTI. The difficulty with this method is in ensuring that the first illuminated pixel read out has been illuminated to the same level as the rest of the image area. If the storage region has a light shield applied it is likely to cover the first few rows of the image area and the alignment will be such that the final row will be only partially shielded. This problem can be alleviated by exposing the image area to flat field illumination before the image and store are both clocked together for a few cycles. The store is then cleared, leaving a well-defined, uniform signal distribution which is then read out as before.

The basic FPER technique has been adapted [99] by using electrical injection and flexible clocking schemes making it more generally applicable.

8 ACKNOWLEDGEMENTS

The drafting of this document has made use of the author’s experience in radiation effects in CCDs, APS and hybrid devices. However, to ensure the document is as complete and as relevant as possible the general community, including users, manufacturers and facilities has been consulted also. Those consulted include Astrium, BAe Systems, CNES, Dalsa, e2v, ESA, ISAE, MBDA, NASA, Onera, The Open University, the Paul Scherrer Institute (PSI), Sodern, Sofradir, SRON and Synergy Health. Particular thanks are due to Andrew Chugg (MBDA), Olivier Gilard (CNES), Vincent Goiffon (ISAE), Dominique Hervé (Sodern), Ruud Hoogeveen (SRON), Thierry Nuns (Onera), Olivier Saint Pé (Astrium), Christian Poivey (ESA) and Cedric Virmontois (CNES). The input and encouragement from Cheryl Marshall (NASA GSFC) is especially appreciated.

APPENDICES

A1 OVERVIEW OF THE SPACE RADIATION ENVIRONMENT

A detailed description of the space radiation environment is given in an ECSS document [39] and has been covered in various short courses provided, for example by Janet Barth [40] and Eamon Daly [41]. Only the principle points are covered here.

The space radiation environment is complex. The radiation received by the spacecraft is dependent on the orbit it is in and on the solar activity during the mission. Damaging radiation within the space environment arises from particles trapped in belts surrounding the Earth or other planets, protons and other heavy nuclei emitted during solar particle events and galactic cosmic rays.

The radiation belts surrounding the Earth consist principally of electrons up to an energy of a few MeV and protons of up to several hundred MeV and are trapped in the Earth's magnetic field. The particle motions are complex and consist of gyration about field lines, a reflection near the Earth's poles, and a drift motion around Earth. There are at least two belts. The inner belt extends from around 100 km altitude to approximately 6000 km. Here the population consists of the high energy protons and medium energy electrons. The outer belt extends out to around 60000 km and consists mainly of the high energy electrons.

For low altitude, low inclination missions the radiation environment is often dominated by the so called South Atlantic Anomaly (SAA). This is an area of enhanced radiation caused by the offset and tilt of the geomagnetic axis with respect to the earth's rotation axis.

When considering displacement damage in terrestrial orbits of greatest concern is that of the effect of protons. However, the displacement damage caused by the high energy electrons in Jovian orbits [42], for example, can be significant.

A2 PARTICLE TRANSPORT AND SECONDARY PARTICLE MODELLING

An important activity in the early phases of the development of an instrument is establishing the radiation environment to which the image sensor is exposed. This is clearly dependent of the orbit and launch details of the mission together with the shielding configuration. Shielding will tend to reduce the low energy components of the proton flux. An example of the calculated mission proton fluence for a typical low earth orbit is shown in Figure 13. This has been calculated using ESA's Space Environment Information System, SPENVIS [43], a comprehensive online suite of tools. A useful offline freeware tools set, OMERE, has been released by TRAD [44] and commercial packages are available also (for example [45]).

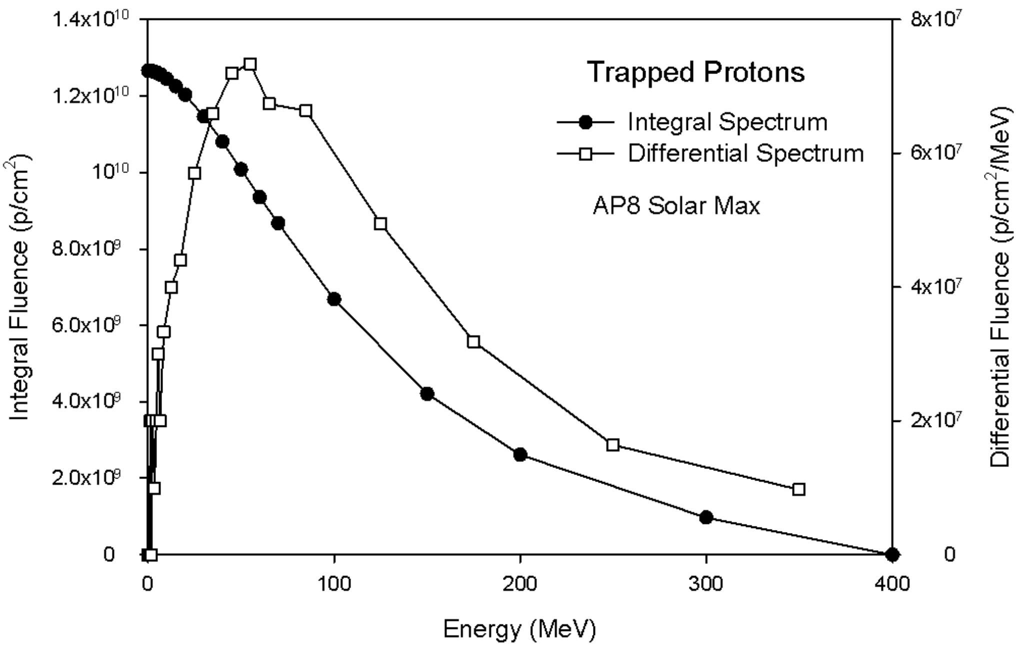

Figure 13 Proton fluence through 10mm of aluminium shielding calculated using SPENVIS. 7 year mission in a sun synchronous orbit at an altitude of 700 km MLTN 11am.

In thick or high Z shields, proton interactions can cause the release of a significant fluence of secondary particles, both protons and neutrons. Complex Monte Carlo codes originally created by the nuclear and particle physics community, such as GEANT4, can be used to track the generation and path of these secondaries. Fortunately a simplified interface to GEANT4, MULASSIS [46], has been developed and is suitable general use by the radiation community. It can be accessed as part of the SPENVIS suite and tracks the passage of each incoming particle as it passes through the shielding material. This can have a user-defined geometry and multiple layers of different materials.

A useful tool available for the calculation of the effect of the interaction of incident protons with the imager is the Monte Carlo code SRIM [2]. The code tracks the interaction of the incident beam with the target material and follows the resultant knock-on target atoms and the ionising and non-ionising energy deposited, and is useful in determining the damage profile through the detector material. In addition to providing details of the interactions within the device being irradiated it is also a useful tool for the calculation of the effect of beam degraders or any window material on the transmitted proton spectrum during an irradiation campaign. SRIM utilises fairly simple models for the estimation of the damage. It does not provide details of the nuclear elastic and inelastic interactions, so if these details are to be investigated other tools, such as GEANT4, need to be employed.

A3 OVERVIEW OF 2D IMAGER TECHNOLOGY

A3.1 Charge Coupled Devices

The main imaging technology of choice for UV, visible and NIR imagers has been the charge coupled device (CCD), and remains so for many applications. An outline of the technology is given in this section. For details of the physics and operation of CCDs the reader is referred to the many publications available (for example [47], and [48]).

In essence the primary structure of a CCD comprises an array of MOS or MNOS type capacitors[1] on which signal charge, generated by interacting photons or other ionising particles, is collected. A typical structure is shown in Figure 14.

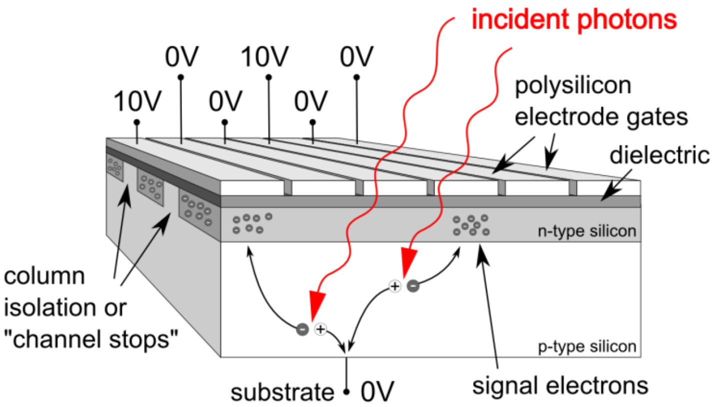

Figure 14 The basic structure of an n-channel CCD showing signal charge being collected under the gates having the high potential.

Following the period of integration the potential between the gate electrodes is changed with a sequence enabling the generated signal charge to be clocked out of the array. This is known charge transfer, the principles of which are demonstrated in Figure 15. As the charge has to be clocked through many electrodes it is essential that the transfer process occurs as efficiently as possible else signal charge may be left behind, leading to a degradation of the acquired image. The lattice mismatch between the SiO_2 of the gate dielectric and the silicon produces a large number of trapping sites which can hinder charge transfer. Early devices suffered from poor charge transfer as signal charge was transferred at the silicon-SiO_2 interface. These devices are known as surface channel CCDs. The introduction of the buried channel CCD eliminated this problem by moving the charge transfer channel away from the interface and into the bulk silicon. This was achieved by introducing an n-type implant, the buried channel implant, into a p-type substrate and ensuring the buried channel is depleted. The resultant potential profile through the silicon, for typical processing parameters, is shown in Figure 16. Signal charge is collected at the potential minimum and held away from the interface during the charge transfer process. Thus charge transfer for a buried channel CCD is significantly better than for a surface channel device. Even so, CCDs manufacturers have to ensure defects and impurities within the bulk silicon are kept at extremely low levels else they will hinder the charge transfer process. Displacement damage due to radiation will also generate trapping sites within the bulk silicon. This degradation mechanism is discussed in Appendix A6.3.4.

[1] Niche x-ray applications have also employed “pn diode” based CCDs

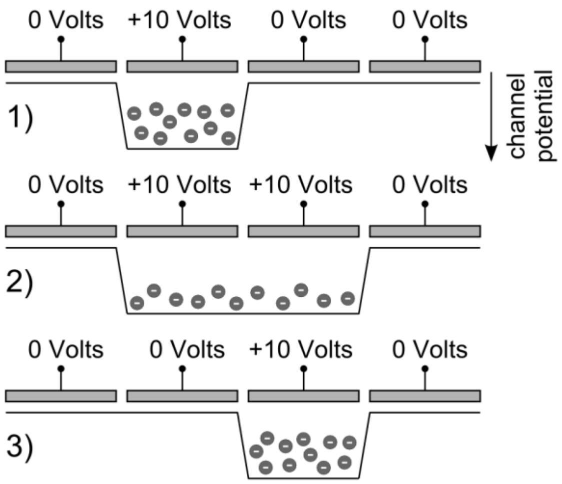

Figure 15 The principle of charge transfer in a CCD showing, schematically, the potential well within the buried channel of the device.

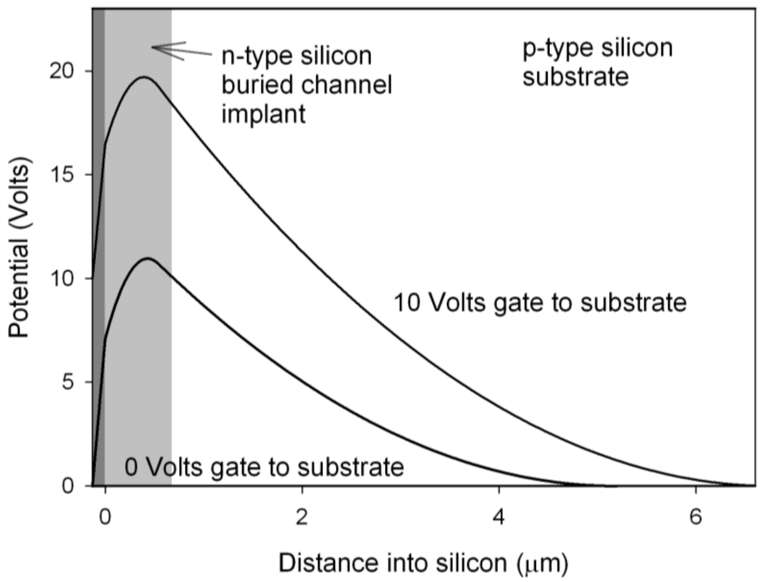

Figure 16 The potential profile through a typical buried channel CCD biased with 0 Volt and 10 Volt gate to substrate potential

The most basic CCD format is known as a full frame (FF) array, illustrated in Figure 17. Here, once integration of signal charge is complete, biases are applied so that all rows are clocked down through the device in a parallel fashion and one row of signal charge is transferred to the readout register. The readout register is then clocked so that the entire signal in the row is moved serially out of the device, via the on-chip charge to voltage conversion circuitry. The sequence of parallel and serial transfer is repeated until all the integrated signal is readout. The device can then be set to integrate the next image. This architecture is employed when a shutter arrangement can be used to prevent light from impinging onto the device during readout, which would otherwise result in a smeared image. When a shutter is not feasible architectures such as the frame transfer, interline or interline frame transfer formats may be employed. For earth observation applications an architecture similar to the full frame array may be used and operated in a time delay and integrate mode. In this case no shutter is required as the parallel clocking is synchronised with the image being scanned across the device.

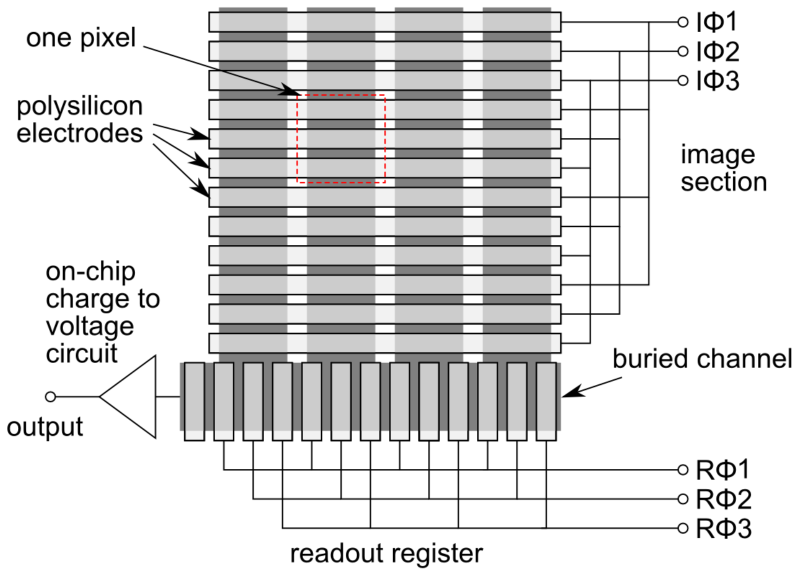

Figure 17 The basic full frame CCD architecture

Figure 17 represents a device having a 3-phase architecture. This means that three electrodes are used to define a row of pixels and three clocking phases are needed to transfer charge from one row to the next. Other architectures are available. For example 4-phase devices have the advantage of an increased signal handling capacity at the expense of increased drive complexity. By utilising a more complicated manufacturing process 2-phase devices can be produced. These are significantly simpler to clock at the expense of somewhat lower maximum signal capability.

Once the signal charge has been clocked through the array it has to be converted to a signal potential. The usual method employs a floating diffusion to create a small capacitance (the output node) onto which the signal charge is transferred. A typical, single stage output circuit is shown in Figure 18. Before signal charge is moved to the node its potential is reset by pulsing the gate of the reset FET. Signal electrons are then clocked onto the node and its potential falls in proportion the charge. The potential is buffered by the on-chip single or multiple stage source follower based circuitry and then sampled by the off chip electronics. Before the charge in the following pixel is transferred to the node the node is reset as before and the sequence continues. Various signal processing techniques can be applied to optimise the noise performance of the output. For example, correlated double sampling is used to eliminate the noise associated with the resetting of the node potential.

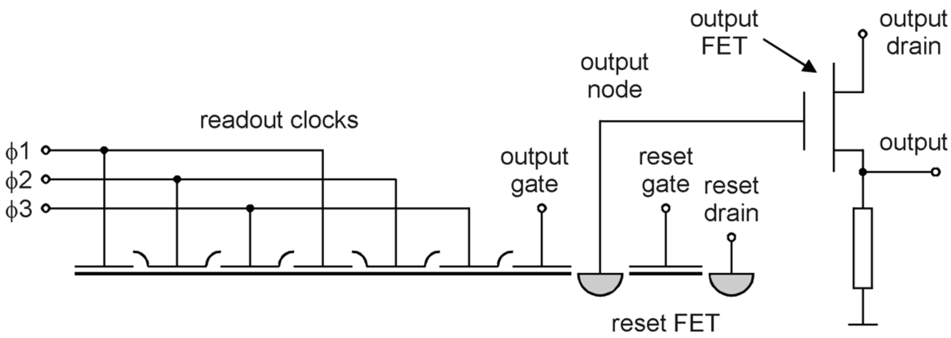

Figure 18 Typical CCD output circuit employing a single stage source-follower

This discussion has focused on n-channel CCDs where electrons are collected and transferred as signal charge, which is the case in the vast majority of devices available. If the device is manufactured on an n-type silicon substrate with a p-type buried channel, and the polarity of the applied biases changed, the CCD will collect holes as signal charge. These are known as p-channel devices and may have some advantages when it comes to tolerance to displacement damage. These are discussed in Appendix A6.3.4.

A3.2 CMOS Image Sensors

The term CMOS image sensor (CIS) covers a broad range of imaging devices based on the complimentary-metal-oxide-semiconductor device technology. Nowadays most CMOS imaging devices are active pixel sensors (APS) in which each pixel includes photo-detector and an active amplifier or buffer circuitry. These have also been referred to as monolithic active pixel sensors or MAPS.

The photo-detector element for a CMOS image sensor is either a photodiode or a photogate structure, as shown in Figure 19. The photodiode structure can be enhanced by adding an additional p+ layer at the surface to create a pinned photodiode, eliminating the dark signal from the interface and improving the tolerance to ionising radiation.

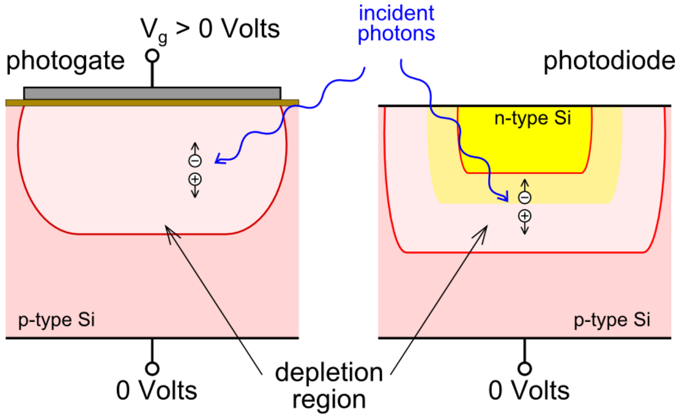

Figure 19 Schematic representations of the photogate and photo diode detector elements

In addition to the photo-detector and any additional circuitry for amplification/buffering within the pixel a CMOS image sensor comprises scan registers to address the sensor line by line and to address each pixel in a line. The architecture of a typical CMOS image sensor is given in Figure 20.

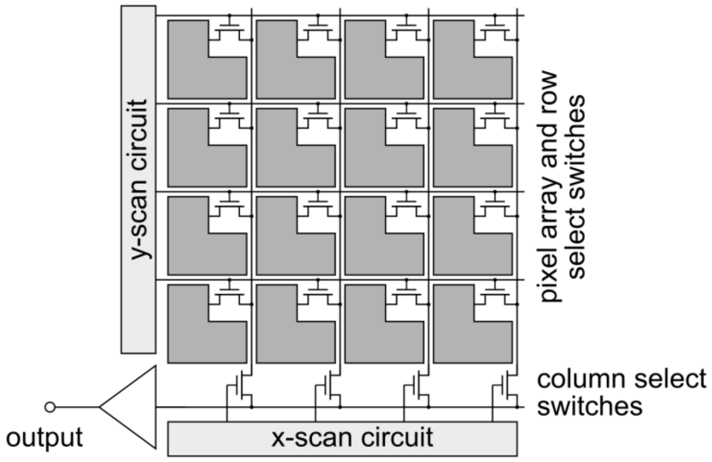

Figure 20 The basic architecture of a typical CMOS image sensor.

There are two basic types of pixel circuitry, one containing three transistors, the other four. These are known as 3T and 4T pixels respectively. Other, more complicated architectures are available to increase functionality. For example, a 5T pixel enables a global shuttering operation. Typical 3T and 4T pixels are illustrated in Figure 21.

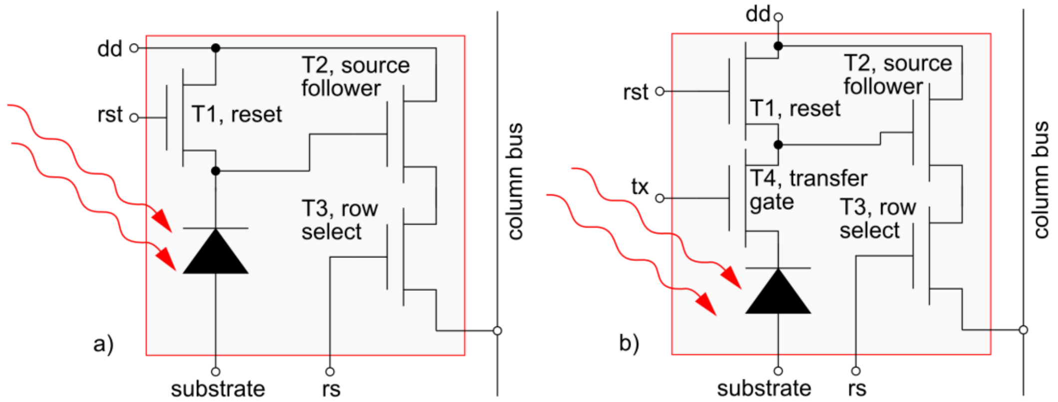

Figure 21 3T (a) and 4T (b) pixel structures. The connection dd is a DC bias, rst, rs and tx are the reset, row select and transfer clocks respectively.

The 3T pixel illustrated in Figure 21a) operates by first resetting the reverse bias across the photodiode to the bias applied to dd by pulsing the gate of T1, the reset FET. Signal electrons generated by the incident photons accumulate on the photodiode, dropping the potential across its capacitance. At the end of this integration period the pixel is addressed by turning on T3, the bias across the capacitance being buffered by the source follower, comprising T2 and a load on the column bus. The 4T pixel shown in Figure 21b) operates in much the same way as a CCD output circuit. Photo-generated electrons are collected onto a pinned photodiode or photogate during the integration period. At the end of exposure the readout node (i.e. the gate of T2) is reset to the potential applied to dd. The first sample is taken after this reset operation. The signal electrons occupying the photodiode/photogate are then transferred to the output node by turning on T4, the transfer gate. A second sample of the output potential is taken after this transfer and the difference between the two samples provides the signal level thus eliminating reset noise.

Because direct transfer of charge is limited, degradation of image quality by charge trapping is of little concern when using with CMOS image sensors in a radiation environment. However, displacement damage can be relevant. The main degradation caused by displacement damage is in the increase in dark signal and particularly the generation of pixels having high levels of dark signal (dark signal spikes) or those having unstable dark signal levels (random telegraph signals). These effects can be exacerbated if high field regions are present within the pixel structure. These mechanisms are discussed in Appendix A6.3.

A3.3 Hybrid Technology

The CMOS image sensors described in the previous section are manufactured on a single silicon wafer, diced then packaged. Both the detection and sampling/amplification of the signal is accomplished on the same silicon die. There can be advantages in separating out these two functions by combining an array of detector elements with a silicon readout integrated circuit (ROIC) typically using indium bump bonding techniques. In this hybrid technology the detector elements and ROIC can be optimised separately. This approach has been used for silicon p-i-n photodiode arrays and is commonly utilised in infrared focal plane arrays, such as those using HgCdTe or InGaAs as the detector layer, illustrated in Figure 22.

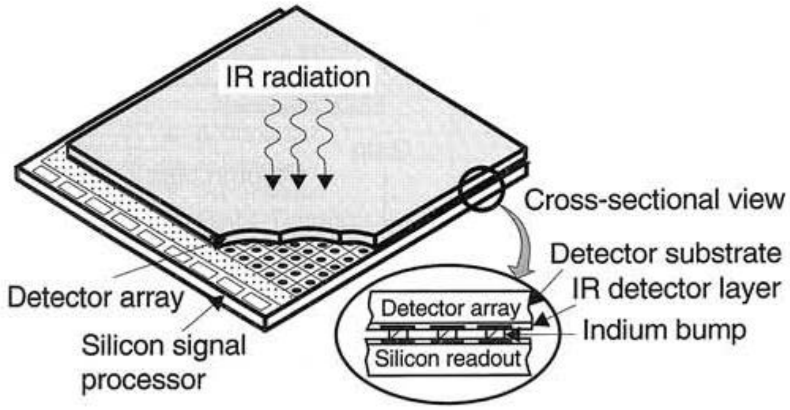

Figure 22 Hybrid imaging array (after [49])

Signal charge is generated in the detector material and collected on diode elements. This charge is then sensed by the underlying pixel circuitry where one of several types of amplifier is used for each pixel [50], for example direct injection, the source follower, the capacitive transimpedance amplifier (CTIA) or the buffered direct injection (BDI) circuit.

In common with CMOS image sensor technology, the main displacement damage issues observed in hybrid arrays tend to be the increase in dark signal and the generation of dark signal spikes in the detector layer. Random telegraph signals are also of concern but, in some cases, especially for IR arrays, the relatively high levels of dark signal generating defects in the pre-irradiated devices can mask the degradation due to displacement damage.

A4 DISPLACEMENT DAMAGE: BASIC MECHANISMS

Particles lose energy by a variety of interactions on passing through material. Those interactions which result in the excitation of atomic electrons are known as ionisation energy loss mechanisms. The non-ionising energy loss (NIEL) mechanisms are those in which the energy transferred by the incident particle results in lattice vibrations (phonon generation) or atomic displacements. The interaction of a charged particle will result in a significantly higher energy deposition by ionisation than by atomic displacements. Even so, the displacement damage generated can have a significant impact on the performance of image sensors.

Displacements occur when the primary interaction results in the displacement of the recoil atom from its lattice position. The primary knock-on atom (PKA) leaves a vacancy creating a vacancy interstitial pair otherwise known as a Frenkel pair. For high energy collisions, the PKA can collide with other lattice atoms, creating more vacancies and interstitial atoms. Some of these point defects are isolated, but for recoil energies much higher than the displacement threshold energy, cascading displacements will occur within a small volume creating a closely spaced group of defects (the so called cluster), especially at the end of the range of the heavy recoil.

To a reasonable approximation the PKA can be displaced only if the transferred energy is higher than a threshold energy, T_d. In silicon this is in the order of 25 eV and the threshold for the production of clusters is ~5 keV [51]. Considering high energy electron irradiation and employing relativistic kinematics the maximum energy that can be transferred to a nucleus of mass *M* by an electron of energy *E* is given by

$$T_m = \frac{2\left(E + 2m_e c^2\right)E}{Mc^2}$$

where m_e is the electronic rest mass. A 1 MeV electron will transfer a maximum of 155 eV to a silicon atom. Thus simple Frenkel pair defects can be created but there will be no clusters generated. Co^{60} irradiation causes damage chiefly through the secondary electrons produced through the Compton interaction. These Compton electrons have a maximum energy of around 1 MeV and so the primary defects created by Co^{60} irradiation will be of a similar nature as those from direct electron irradiation.

Protons and neutrons have a mass that is around 2000 times greater than the mass of an electron. Therefore, for energies below about 100 MeV, classical mechanics can be used to calculate the maximum energy that can be transferred to the target nucleus through elastic scattering. In this case

$$T_m = \frac{4mM}{(m+M)^2}E$$

where *m* is the mass of the proton or neutron. A 1 MeV proton or neutron will transfer a maximum energy of 133 keV to the PKA which is significantly greater than the threshold required for cluster generation.

As protons and electrons are charged, the scattering is coulombic and can be described by the Rutherford cross section, modified for relativistic effects where necessary. The total cross section for displacement is in the order of 5×10^{-20} cm^2 for a 5 MeV proton, around 3 orders of magnitude greater than the cross section for a 5 MeV electron, which implies that the protons are significantly more likely to cause displacements than the electrons for the energies likely to be encountered in space. For coulombic scattering the mean energy transferred to the PKA is given by

$$\bar{T} \approx \frac{T_d T_m}{T_d + T_m}\ln\left(\frac{T_m}{T_d}\right).$$

The mean energy transferred to a displaced silicon atom by a 5 MeV proton will be around 250 eV. The primary interaction of neutrons differs from that of protons and electrons as they are uncharged and can be described in terms of hard sphere collisions. The total elastic scattering cross section of light elements is in the order of the geometric cross section of the atomic nucleus ≈ 10^{-24} cm^2. This value is very much less than the cross section for displacement by high energy electrons or protons. Therefore the number of PKAs generated is relatively small. However, ignoring inelastic interactions, the mean energy given to a displaced silicon atom is approximately $T_m/2$. For a 5 MeV neutron this gives 340 keV yielding a significantly higher number of secondary displacements.

Thermal energy enables the radiation induced defects to migrate through the crystal lattice and, eventually, be annihilated by the recombination of the vacancy interstitial pairs or by the creation of stable defects in association with other impurities or defects already present.

The created defects can generate discrete levels within the bandgap of the semiconductor material. They can capture and emit electrons and holes and produces changes in the properties of the semiconductor. An important point defect generated in phosphorous doped n-type silicon is the phosphorous-vacancy complex, otherwise known as the Si-E centre. The primary vacancies and interstitials can also team up with unintentionally added impurities within the material, such as oxygen, to create the Si-A centre or carbon. The divacancy is a stable configuration of paired vacancies and multiple vacancy complexes are also possible.

The energy levels within the band gap and the capture cross sections are a signature of the defect type. Unfortunately, due to experimental uncertainties and systematic errors a wide range of values tend to be presented in the literature. For example, the Si-E centre is reported to have an acceptor level in the range 0.42±0.06 eV below the conduction band edge and the Si-A centre an energy level of 0.17±0.02 eV below the conduction band. The silicon divacancy is more complicated as it is an amphoteric level meaning that it has multiple levels within the band gap relating to the differing charge states namely (--/-/0/+). Two acceptor levels appear in the upper half of the band gap, one in the same range as the Si-E centre associated with the (--/-) transition on the emission of an electron and one at around 0.23 eV below the conduction band corresponding to the (-/0) transition. It also introduces a donor level in the lower half of the band gap at around 0.35 eV above the valence band. A review and detailed measurements on point defects in silicon has been made in [52].

The nature of the defect complexes produced by neutrons and protons are essentially the same as those produced by electrons. In the past it had been thought that the stable cluster complexes caused by neutrons act as extended defects. This has been shown not to be the case [53] and that the displacement damage effects are most readily explained on the basis of stable defects acting as isolated recombination and trapping centres. In clusters it is likely that multi-vacancy complexes exist although to date this has not been confirmed.

A5 ANNEALING

Compared with the annealing of ionisation effects annealing of displacement damage is very different and standard annealing tests (such as described in ESCC22900, RD1) are not applicable. There are three main reasons why one may wish to perform an increased temperature anneal. Looking at the anneal characteristics may help in the identification of the defects involved in the performance degradation process. An anneal procedure may be employed to repair the degradation or it may be used as an attempt to accelerate testing and to try to simulate end of life performance. The last two motivations must be treated with caution. As now discussed, increasing the temperature will lead to a reordering of the defect population responsible for parameter degradation. This may increase the degradation observed or may produce a change in device performance that is not be representative of extended time spent at the operating temperature. This section describes the annealing process and observations on the effect on device performance are made within the following sections.

As discussed in Appendix A4, irradiating particles can cause the creation of vacancies, interstitials, divacancies and possibly clusters. The generation of these primary defects is only the start of the process. Once these have been generated the damage progression continues. Vacancies in silicon are very mobile even at temperatures as low as 20K depending on their charge state. Interstitials are just as mobile and both will migrate through the lattice forming pairs with dopant acceptors or donors or other impurity species present in the silicon. Vacancies can also combine with each other to form divacancies. Higher order vacancy complexes are likely to be important within clusters.

If sufficient thermal energy is given to the silicon lattice then the vacancy or interstitial related defect complex will become mobile and subsequently break up or recombine with other defects, forming a different defect complex. This process is known as annealing. The type of defect or complex determines the temperature at which this occurs, and the time scale of the process. The defect kinetics and reactions are dependent on the concentration of sources and sinks within the material. For example, if the material is p-type silicon with no phosphorous present, then no phosphorous-vacancy complexes (Si-E centres) will be created. Also the diffusion limited process of vacancy transport is strongly depended on the concentration of oxygen. A thorough review of the annealing processes is given in [52] and a schematic representation of vacancy and vacancy pair annealing in silicon is shown in Figure 23. This shows a selection of defect complexes. It is likely that other complexes exist as some of the annealing behaviour observed in image sensors cannot be explained entirely by the data presented here.

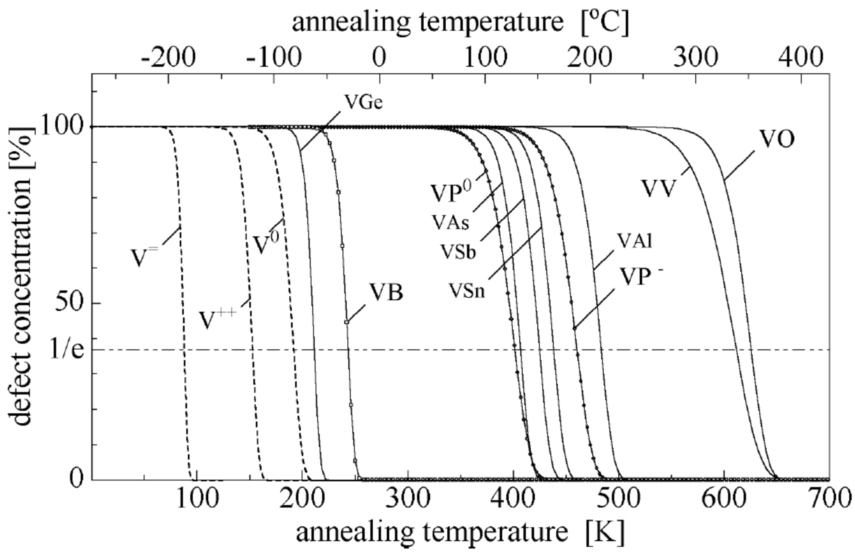

Figure 23 Schematic representation of vacancy and vacancy-defect pair annealing in silicon after [52]

The mobility and breakup of the defects and defect complexes has a couple of implications. Firstly, the stable defects generated when the irradiations are performed warm may not be those relevant to those generated during cold irradiations, possibly leading to a false indication of performance degradation during the operational environment. This situation is discussed in relation to charge transfer degradation of CCDs in Appendix A6.3.4. Secondly, if the temperature of an irradiated device is raised and then returned to the normal operating temperature a degraded device parameter may be improved if that parameter is dependent on a defect complex that anneals out at the elevated temperature. If the reorientation of the defect complexes is unfavourable the result may be seen as degradation in the parameter. This is known as reverse annealing.

A6 EFFECT OF DISPLACEMENT DAMAGE ON 2-D IMAGER PERFORMANCE

A6.1 General Considerations

A general overview of the effects of displacement damage in silicon devices is given in [54] and a comprehensive overview of the effect of radiation from a historical perspective, including displacement damage effects, can be found in [55].

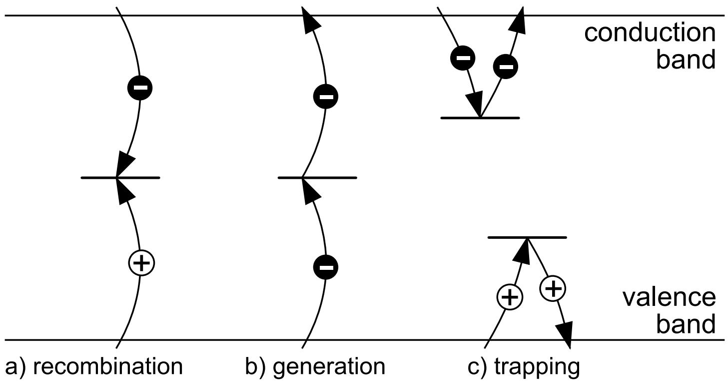

Figure 24 The main effects of radiation induced levels within the band gap

The energy levels within the band gap of semiconductors, due to radiation induced defect complexes, have several effects which are illustrated in Figure 24. Figure 24a) shows the process of recombination. Here a charge carrier is captured at the defect centre and subsequently a carrier of opposite sign is trapped at the same centre. The rate of recombination depends on the density of the centre, the free carrier concentration, the electron and hole capture cross sections for the centre and on the position of the level within the band gap. There are four processes that determine the recombination rate via a single level in the band gap. Those are, electron capture by the level, electron emission from the level back to the conduction band, hole capture by the level and the emission of a hole from the level to the valence band. The total rate of recombination can be calculated using Shockley, Read, Hall (SRH) statistics and is given as

$$R = \frac{\sigma_n \sigma_p v_{th} N_t \left(np - n_i^2\right)}{\sigma_n\left(n + n_i \exp\left(\left(E_t - E_i\right)/kT\right)\right) + \sigma_p\left(p + n_i \exp\left(\left(E_i - E_t\right)/kT\right)\right)}$$

where σ_n and σ_p are the electron and hole capture cross sections, v_{th} is the thermal velocity of the charge carriers (assumed the same for electrons and holes), N_t is the trap density, n and p are the electron and hole densities, n_i is the intrinsic carrier density, E_i is the intrinsic Fermi level and E_t is the energy level of the centre. This rate reaches a maximum when E_t is equal to E_i. Therefore the most effective traps for recombination are situated around the centre of the band gap. The mean time a minority carrier spends in its band before recombining is known as the minority carrier lifetime. Radiation induced recombination centres cause this lifetime to decrease.

In the depletion region of a device n and p are very much less than the intrinsic carrier concentration and, setting the electron and hole capture cross sections equal for illustration, the recombination rate becomes

$$R = \frac{-\sigma v_{th} N_t n_i}{2\cosh\left(\left(E_t - E_i\right)/kT\right)}$$

In this case the rate of recombination is negative indicating that electron hole pairs are being generated. This is the process shown in Figure 24b) and can be viewed as the alternate emission of an electron and hole from the level. Alternately it can be seen as the thermal excitation of a bound electron from the valence band to the level which is then followed by the excitation of that electron to the conduction band. The rate of generation is also a maximum for traps near mid gap. Therefore radiation induced levels near mid gap, in the depletion region of a device, contribute most to the dark current. It has been postulated by Watts et al. [56] that enhancement to the generation rate by over two orders of magnitude can be attributed to intercentre charge transfer between closely spaced defects, especially in the cluster regions of the damage cascade. Defects occurring in high field regions of a device can also show enhanced generation rate due to the Poole–Frenkel effect, or trap assisted tunnelling, for example.

If a charge carrier is captured at a defect centre, and is later emitted back to its band before a recombination event can take place, the level is generally called a trap. The process of an electron being trapped from the conduction band is shown in Figure 24c). Traps caused by radiation are the main cause of CTE degradation in CCDs. A more detailed review of this is given later in this section.

Two further effects can be observed following very high fluence levels but are generally of little importance in image sensors. Defects deep within the band gap can compensate the intentionally introduced dopant atoms. For example, the fixed positive charge introduced by a shallow donor level can be compensated by the negative charge of a deep lying radiation induced acceptor level. The result is a reduction in the equilibrium majority carrier concentration, with the material appearing more intrinsic as far as the carrier concentration is concerned. The charged radiation induced defect centres also act as scattering centres which can be seen in the decrease in the mobility of the charge carriers at very high radiation levels.

A6.2 The Use of NIEL

A6.2.1 Scaling and Performance Prediction

The use of the non ionising energy loss (NIEL) is a useful tool for the interpolation and extrapolation of displacement damage test data taken under a limited set of irradiating particles and energies to the degradation expected within the operating environment. It has been found that many displacement damage effects depend, approximately, only on the non-ionising energy deposited within the sensitive volume of the device and not on the type or initial energy of the particle. A rigorous framework for understanding the NIEL scaling of generated mean dark signal and the effect of cluster damage, for example, is presented in [57].

However, there are problems with the use NIEL. NIEL scaling suggests that the number of initial displacements is proportional to the energy of the primary knock-on atom and the nature of the damage does not change with particle energy. In the cascade regime it is implied that the number of cascades increases with increasing energy. It also means that the electrical effect is proportional only on the concentration of defects and not on the inventory of stable defects created. These implications are generally quite reasonable unless the degraded parameter is dependent on a specific defect type, for example, multi vacancy complexes, which are not generated by particles producing only point defects, or that interaction between closely spaced defect types is important. Some of the issues are discussed in the following sections. Even in the same device type (e.g. a CCD) one may find that one parameter follows NIEL correlation whereas another does not. Likewise it has been found that sensor properties that depend on the minority carrier lifetime may well correlate with the Coulombic portion of NIEL and not on the total NIEL. Also, correlation may work better for properties depending on the generation lifetime. Inguimbert et al. [58] have developed an a approach using an “effective NIEL” to take into account a more complex defect generation process than that usually assumed when using a simple single threshold assumption to vacancy/interstitial creation[2].

Nevertheless it should be emphasised that NIEL scaling is a reasonable first approximation and it removes most of the particle and energy dependence in device damage estimation. This is fortunate as, without the NIEL hypothesis, it would be very difficult to make predictions of device response to a radiation environment. However, the uncertainty in the NIEL scaling approach must be taken into account when dealing with mission margins.

To see how the NIEL can be used to estimate degradation, we define a damage factor , K_{damage}. If a device parameter, P, varies linearly with fluence, ϕ, a damage factor is defined such that

$$P = K_{damage} NIEL(E)\phi$$

[2] A used in the Kichin-Pease approach.

where *NIEL* provides the energy an particle dependence of the degradation to *P*. To predict the displacement damage effects throughout a mission experimental damage factors are required. Caution must be taken here since damage factors may depend on operating conditions and it is necessary to ensure that the damage factors employed are appropriate for the application and that any annealing effects have been acknowledged. Once the expected radiation environment has been modelled to give the particle fluence spectrum $d\phi(E)/dE$ as a function of energy (E), including effects of shielding, the mission damage can be calculated from

$$P_{mission} = K_{damage} \int NIEL(E) \frac{d\phi(E)}{dE} dE$$

Here it is assumed that the device parameter scales linearly[3] with NIEL. If there are doubts then the NIEL curve may have to be extrapolated from experimental measurements at a range of energies although cost and programme constraints may prevent this. If there is a range of particle species present within the environment then the total mission damage will be the sum over the particle population.

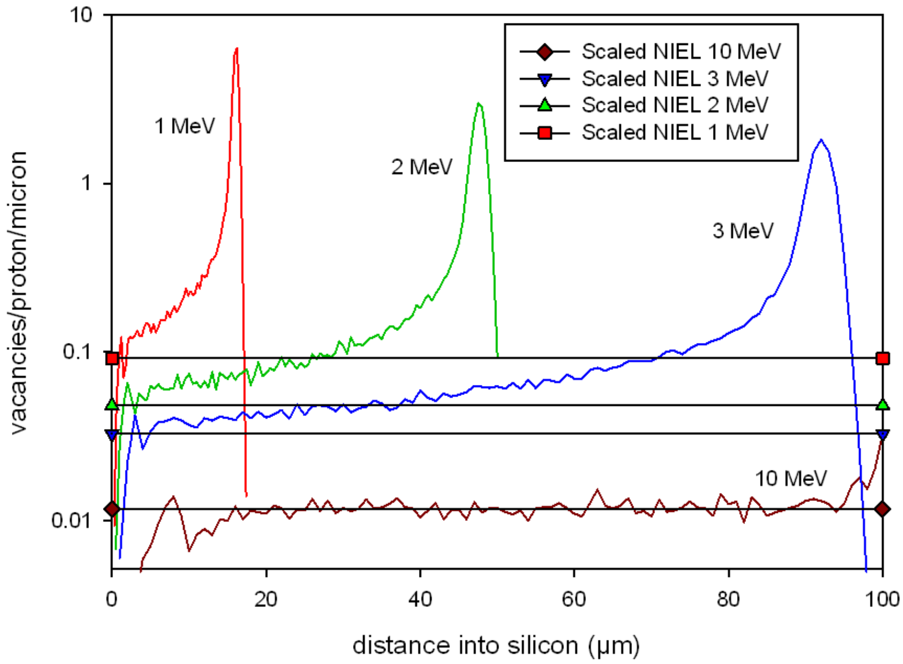

Figure 25 The profile of the damage through silicon calculated using SRIM [2]

When utilising the NIEL concept to estimate the degradation care must be taken to ensure the non ionising dose deposited within the sensitive volumes of the imager are as expected. Problems may arise if the device being tested is being irradiated with particles having a range comparable with the dimensions of the technology. As an example, the output from the SRIM Monte Carlo code is shown in Figure 25. Here the density of generated vacancies is plotted as a function of depth into silicon for a range of incident proton energies. Also in the figure is the NIEL scaled to the mean vacancy density produced by the 10 MeV protons. It is clear that as the proton slows down, towards the end of its track, it becomes more damaging. In a back illuminated CCD the buried channel lies between 10 and 20 microns from the input surface. This is at the end of the range of 1 MeV protons resulting in significantly greater displacement damage than expected by using NIEL alone.

[3] This assumption is reasonable in the case of protons but may breakdown when considering electron radiation for example (see section A6.3).

A6.2.2 Units for NIEL

The NIEL of a particle is usually presented in terms of keVcm^2/g or MeVcm^2/g. Alternatively the NIEL can be specified in terms of displacement damage cross section, expressed in MeVmb. This is popular within the high energy physics community. In silicon 100 MeVmb is equivalent to 2.144 keVcm^2/g.

For a mono-energetic beam, the product of the NIEL and the particle fluence gives the displacement damage dose which is usually specified in units of keV/g or MeV/g. For irradiation by a range of particle energies the displacement damage dose is obtained by integrating the energy dependent NIEL over the particle spectrum. Alternatively a displacement damage equivalent fluence can be defined. This is the fluence of particles at a particular energy that would give an equivalent displacement damage dose. Often 10 MeV protons or 1 MeV neutrons are given as the reference particle.

A6.2.3 Values of NIEL

The values for the NIEL of various particles in silicon have been published by, for example, Dale et al. [59], Huhtinen et al. [60], Akkerman et al. [61], Summers et al. [62] with an online compilation by Vasilescu and Lindstroem [63]. Values are summarised in Figure 26. Various calculations tend to agree within a factor two which is comparable with the uncertainties involved.

Values for InGaAs have been published by Walters et al. [64] and Fodness et al. have published results for HgCdTe [65]. Jun et al. have published results for protons in a range of important semiconductor materials [66] and also for electrons [67].

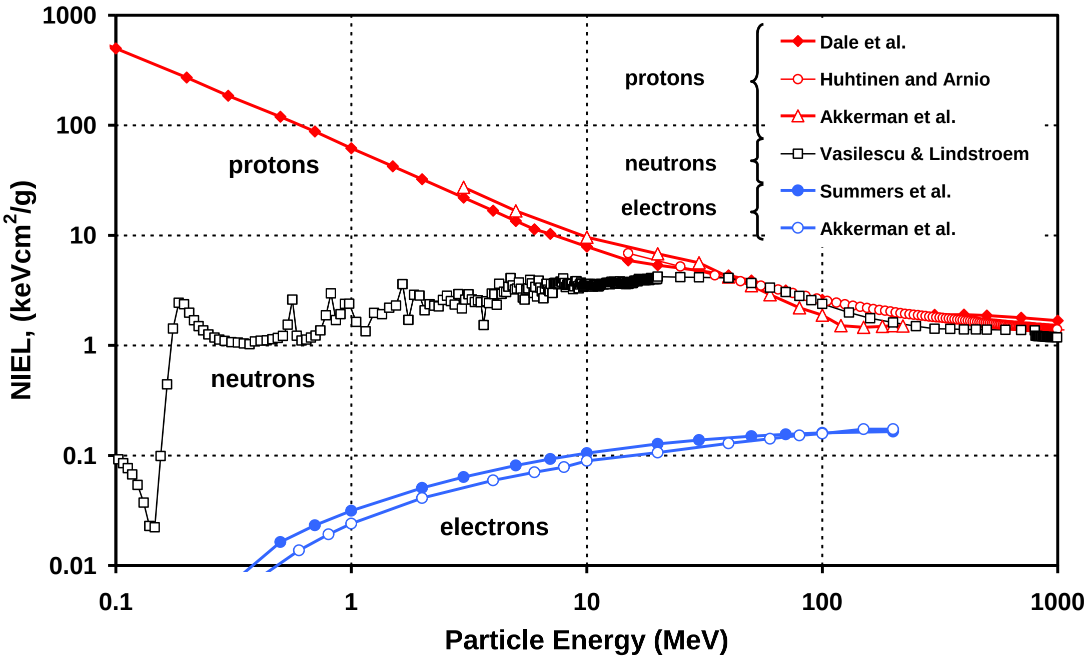

Figure 26 Some of the published values of NIEL in silicon

SPENVIS [43] includes several models for the NIEL of protons in Si, GaAs and InP for the calculation of damage equivalent dose for a user defined mission. The software suite OMERE [44] provides NIEL curves for protons and electrons for any material having an atomic number less than 84. These NIEL values are calculated using an internal model, NEMO [68,69]. NIEL values are also calculated for neutron energies greater than 1 MeV.

A6.3 Device Degradation

A6.3.1 Dark Signal

A radiation environment can cause an increase in thermally generated signal, known as dark signal or dark current. Both ionising and displacement damage increases dark signal. Ionisation damage results in an increase in the density of generation centres at the semiconductor/dielectric interfaces and thus an increase in dark signal if these interfaces are depleted. This is often referred to as surface dark signal. In most space radiation environments this source of dark signal will dominate the degradation in the dark signal observed unless it is suppressed, for example, by eliminating depleted surfaces from the pixel structure or by flooding the surface with charge carriers, as in the case of inverted mode operation of CCDs.

If the ionisation induced dark signal is suppressed efficiently, an increase in dark signal caused by the generation centres introduced by displacement damage will be observed. This is often known as bulk dark signal. The dark signal per pixel is dependent on the density of generation centres within the bulk material, the depleted volume associated with each pixel and the temperature. As noted in section A6.1 the most effective generation centres are those having an energy level close to mid gap. For a mid gap generating centre the theoretical variation of dark signal with temperature is given by

$$I \propto \sqrt{T}\, n_i \propto \sim T^2 \exp\left(\frac{-E_g}{2kT}\right)$$

where n_i is the intrinsic carrier density, E_g is the band gap and k is the Boltzmann constant. Note that the pre-exponential term is T^2 compared with a T^3 in the case of generation by interface states.

The mean level of bulk dark signal in silicon devices has been found to scale approximately with NIEL [70]. Work performed on CCDs [71], looking at dark signal degradation caused by 10 and 60 MeV, protons presented the following relationship

$$\Delta s \approx 10^{-5} \times V \times \phi \times NIEL \times T^2 \exp\left(\frac{-6628}{T}\right)$$

where Δs is the mean dark signal increase in electrons per pixel per second, V is the depletion volume of the pixel in µm^3, Φ is the proton fluence in cm^{-2} and NIEL is the non ionising energy loss measured in keVcm^2/g. The temperature dependence was measured over a temperature range of 274K to 298K.

A general expression for the bulk dark signal has also been proposed in [72]. Here a dark current damage factor was defined as

$$K_{dark} = \Delta G / D_d$$

where ΔG is the radiation induced increase in the rate of electron-hole pair generation and D_d is the displacement damage dose (particle fluence x NIEL). From a literature survey the damage factor was found to be

$$K_{dark} = (1.9 \pm 0.6) \times 10^5 \text{carriers/cm}^3\text{/s/(MeV/g)}$$

at 300K and is entirely consistent with the results presented in [71]. This universal damage constant and linear scaling of the mean dark signal with NIEL was found to hold over a range of irradiating species providing there was a high probability introducing cluster damage. For electron irradiation having a low probability of cluster creation the increase in dark signal followed a quadratic dependence on NIEL. This has been discussed in detail in [57].

The relationships above are very useful for the prediction of the increase in dark signal from silicon devices. However, work is ongoing in this area and there is some evidence ([73] and [74]) that higher energy protons are slightly more effective at causing dark signal increase compared with the actual NIEL scaling. Also, to use the relationships the volume of depleted silicon within a pixel is needed and this is not always available from the supplier.

Following room temperature proton irradiation of silicon CCDs a significant reduction of bulk dark signal at annealing temperatures greater than 100 ^{o}C has been observed, for example in [73]. The defect or defect complexes responsible for the dark signal generation are not likely to be impurity related due to the ability to apply a universal damage constant [71 and 72] to the dark signal. It is also not likely to be dominated by the divacancy as this would require temperatures in excess of 300^{o}C to anneal significantly. Watts et al. [56] have shown that the dark signal from neutron irradiated silicon is dominated by three defect species having an energy level around that of the divacancy, including possible contribution by the V_4 complex which has the anneal behaviour observed.

Room temperature annealing of bulk dark signal in silicon devices does occur as illustrated by Figure 27 presented by Srour [54]. Recent measurements made on CCDs have shown an unexpected bias dependence to the annealing behaviour [AD-2]. Further work is required to fully characterise and understand the annealing behaviour.

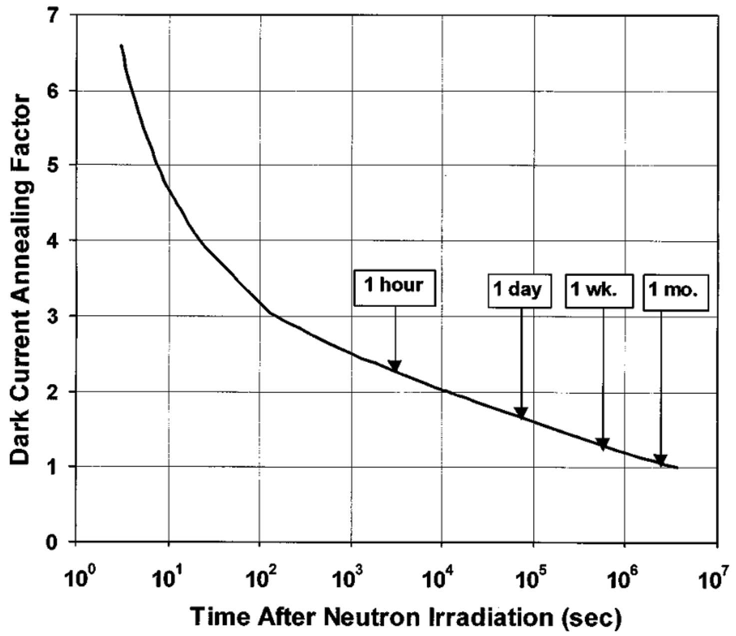

Figure 27 The bulk dark signal from a CCD at room temperature following neutron bombardment [54]. The dark signal is normalised to the dark signal after 1000 hours.

There is only limited data on the increase in dark signal from infrared imagers within the public domain and no "universal" damage constant has been established to date. Complications arise due to the range of band-gaps available for a particular material type, depending on the wavelength requirements of the imager. Some work on InGaAs photodiodes, for example [75] and [76], has shown that the increase in dark current and a decrease in photocurrent is caused by an increase in deep levels. Bulk dark signal increase was the main degradation observed in InGaAs detectors used on the SPOT 4 satellite [8]. Within experimental uncertainty, the mean dark signal was seen to scale with NIEL over the range of proton energies employed (9.1 MeV to 300 MeV). The damage factor for the devices irradiated at room temperature, and measured at 5^{o}C, was found to be 2.32 x 10^{-5} nA g/MeV/cm^2. The temperature dependence was given by

$$\text{Dark Current Density} \propto \exp\left(\frac{-0.44\ eV}{kT}\right)$$

This is in reasonable agreement with the temperature dependence expected for a mid gap level (the band gap noted as ranging from 0.75 eV to 0.79 eV). The devices measured in [8] utilised a CCD type readout requiring the InGaAs photosite to be reverse biased. However, further work showed that if operating at zero bias, significantly improved radiation tolerance, both in the mean dark signal and dark signal spike generation, can be achieved. Therefore, low degradation can be accomplished, for example, by utilising a capacitive transimpedance amplifier (CTIA) pixel readout which enables near zero biased operation [77].

Most work has been performed on InGaAs material lattice matched to the InP substrate. However, the NIR channels of the SCIAMACHY instrument on board ESA's ENVISAT utilised both lattice matched and extended wavelength InGaAs detectors. The wavelength extension was achieved by varying the fraction of Indium and Gallium, creating a lattice mismatch between the detector material and the substrate. In flight data has been analysed in detail [78]. The number of defective pixels, attributed to an increase in displacement induced dark signal, increased throughout the mission life. However, this increase was not observed in the lattice matched devices. Commercial lattice matched and extended wavelength InGaAs devices have been tested for the ESA EarthCARE mission [79] no displacement damage changes were observed up to a 60 MeV proton fluence of 1.5 x 10^{10} cm^{-2}. However, this may have been due to the effects of any radiation induced defects being masked by the large numbers of pre-existing defects.

Work on short wavelength HgCdTe detectors (1.7µm cut-off) has been reported following evaluation for the Wide Field Camera 3 of the Hubble Space Telescope [80]. Irradiations were undertaken at a temperature of 150K and measurements were made before the devices were warmed up. In addition to observing the proton stimulated luminescence from the CdZnTe substrate an increase in proton induced dark signal was seen. Initial increase decayed to a stable level a few times the preirradiation value following a 63 MeV fluence of ~5x10^9 p/cm^2. Some annealing of this dark signal was observed when the devices were warmed to 190K and complete recovery was achieved by annealing the devices at room temperature.

Proton irradiation of an HgCdTe focal plane array for use in the 8-15 µm spectral range has been reported in [81]. Here devices were irradiated at a temperature of 55K to a fluence of 10x10^{10} 50 MeV protons per cm^2. An increase in the median dark signal of ~0.5 mA/cm^2 was observed. A subsequent 2 month room temperature anneal reduced this to close to the preirradiation figure and most of the high dark signal "spikes" annealed out. A 168 hour anneal at 70^{o}C returned the device to its pre irradiation state.

A6.3.2 Dark Signal Non-Uniformity and Defective pixels

Dark signal non-uniformity (DSNU) is the variation in the mean dark signal from one pixel within the imaging array to the next. A variation naturally occurs due to the statistical spread of deposited energies by the irradiating particles. The theory of proton interactions in silicon within the microvolume of a pixel forms the basis for predicting the DSNU in silicon devices. This has been discussed in detail by Dale et al. ([82], [83] and [84]) with a later modification of the models by Robbins [71]. The shape of the distribution of dark signal generation rates is dependent on the proton energy and fluence and the depletion volume of the pixel. Providing field effects are not significant changing the temperature will simply change the mean dark signal (as noted in the previous section) and the distribution scaled accordingly. Examples of the calculation using the approach taken in [71] are shown in Figure 28 and Figure 29. At high proton energies (>60 MeV or so) Monte Carlo codes are required to account for the correlation of damage between pixels when the recoil ranges are comparable to the pixel volume [5].

The dark signal distributions cannot always be explained by the interaction kinematics alone. In some devices the electric fields within a pixel can be sufficiently high that the emission rate from bulk defects can be enhanced significantly (e.g. [85]). A characteristic of this phenomenon is that the dark current non-uniformity changes more slowly with temperature. In many cases, there is a clear correlation between the size of a dark current spike and the decrease in activation energy. It can be difficult to predict the evolution of the dark signal distributions throughout a mission lifetime, including enhancement effects. One approach, using experimentally determined distributions obtained for a few proton energies, has been presented by Gilard et al. [86,87].

CCD pixels having high levels of dark signal (hot pixels or dark signal spikes) following irradiation at -84 ^{o}C have been investigated by Marshall et al. [59]. Hot pixel annealing began at temperatures below -40 ^{o}C and was completed before the temperature reached +20 ^{o}C. Low temperature irradiation of a CMOS APS by alpha particles was seen to increase the number of dark signal spikes of which 90% were annealed following a few hours at room temperature [15].

A similar approach to that used for the modelling of dark signal non-uniformity in silicon devices has been applied to HgCdTe arrays [88]. There was a significant discrepancy between calculated distributions and those measured. This may be attributable to field enhancement effects.

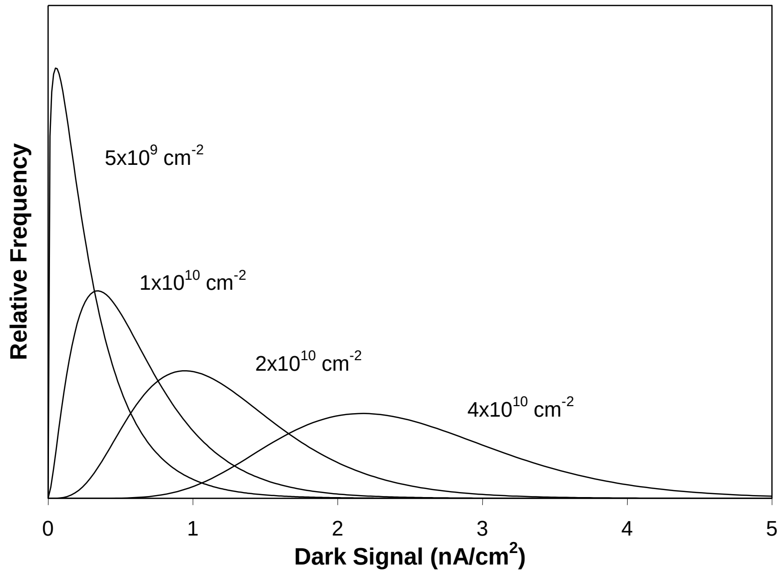

Figure 28 Calculated dark signal distributions for a silicon device following 10 MeV proton irradiation over a range of fluences. The temperature was 300K and with a depleted pixel volume of 387 μm^3.

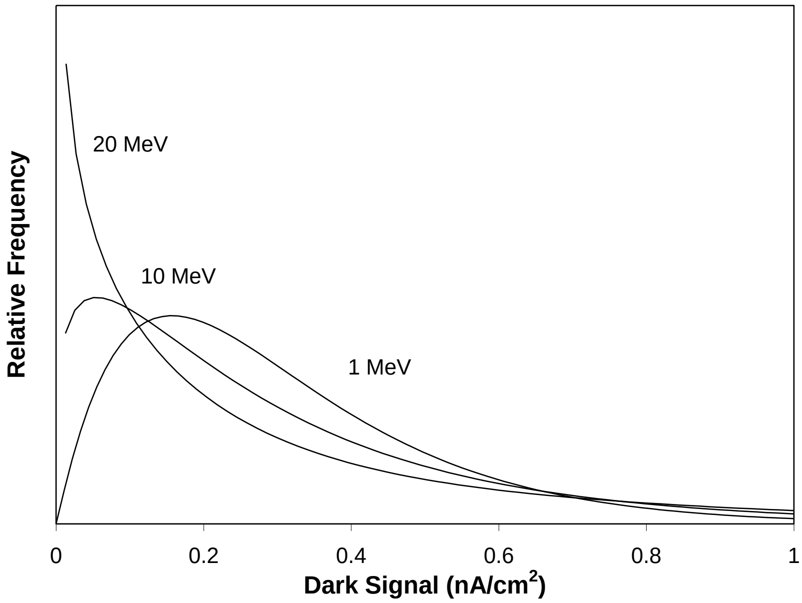

Figure 29 Calculated dark signal distributions for a silicon device following proton irradiation showing the effect of proton energy. In all cases the 10 MeV equivalent fluence was 5x10^9 cm^{-2} and the mean dark signal increase was 0.3 nA/cm^2. The temperature was 300K and with a depleted pixel volume of 387 μm^3.

Figure 28 and Figure 29 show smooth distributions as observed at relatively low dark signal levels. At long integration times some structure in the distributions can be seen and relates to the generation from the discrete generation centres [16].

A6.3.3 Random Telegraph Signals

Random telegraph signals (RTS) in image sensors refers to two distinct phenomena. Firstly, it could refer to the switching between discrete current levels within the channel of the MOSFETs in the readout circuitry. This is particularly relevant to the small source follower FET in the deep sub-micron technology used in CMOS active pixel sensors and results from carrier trapping and detrapping from levels within the oxide or bulk semiconductor. Displacement damage could affect this but to date this damage mechanism appears to be of minor significance. The second and distinctly different phenomena, is the switching between high and low dark signal generation rates observed within, or surrounding the depletion volume of the charge collection regions. Some pixels in an image sensor array may show this behaviour prior to irradiation but displacement damage can cause a significant increase in number. Typical RTS behaviour following proton irradiation is shown in Figure 30. RTS generating centres have been shown to be introduced by ionisation damage also [89]. However, ionisation induced RTS transitions have amplitudes somewhat lower than the RTS defects generated by displacement damage [90].

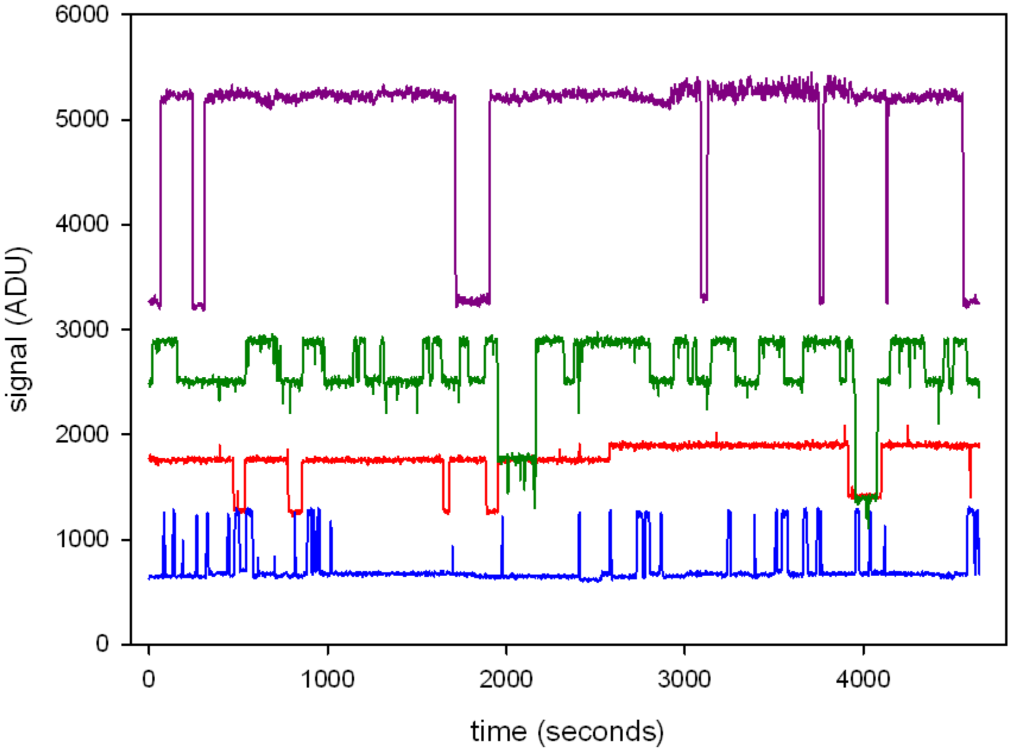

Figure 30 A sample of 3 CCD pixels showing RTS behaviour at 23°C. Similar RTS behaviour is seen in CMOS image sensors.

Most of the investigation into displacement damage induced RTS phenomena has been undertaken on silicon devices. Work performed in [74] showed that the characteristics of the radiation induced RTS dark signal observed in CCDs and APS imagers following proton irradiation was very similar. Over the range of proton energies tested (1.5 to 60 MeV) the number of RTS pixels scaled with displacement damage dose, derived from the total NIEL, with both elastic and inelastic interactions possibly contributing [32, 85].

The numbers of RTS pixels detected depends on the method of detection employed, and care must be taken when comparing results. A detailed study of RTS pixels from CMOS APS devices using a sophisticated detection technique [32] showed that many of the high dark signal pixels presented RTS behaviour. The number of RTS pixels is dependent on the number of pixels in the array, N_{pix}, and the volume of depleted silicon in each pixel, V. The number obtained from data in [32] is

$$N = 47 \times N_{pix} \times V(\mathrm{cm}^3) \times Fluence(\mathrm{cm}^{-2}) \times NIEL(\mathrm{MeVcm}^2/\mathrm{g}).$$

Following the proton irradiation of a CCD presented in [74] the fraction of RTS pixels was found to be

$$N/N_{pix} \approx 8.1 \times 10^{-3} \times A(\mathrm{cm}^2) \times Fluence(\mathrm{cm}^{-2}) \times NIEL(\mathrm{MeVcm}^2/\mathrm{g})$$

where *A* is the pixel area. As the device tested was run in inverted mode the depletion depth would have been around 3 µm. Therefore

$$N/N_{pix} \approx 27 \times V(\mathrm{cm}^3) \times Fluence(\mathrm{cm}^{-2}) \times NIEL(\mathrm{MeVcm}^2/\mathrm{g})$$

which is in very good agreement with the data of [32] considering the uncertainties involved.

If a pixel shows RTS behaviour it may have 2 levels or multiple discrete levels of dark signal generation. Significantly higher numbers of multiple level RTS pixels are observed (e.g. [74] and [91]) than would be expected through the statistical distribution of 2 level defects. The maximum RTS transition in a pixel has been found to have an exponential distribution [32] given by

$$F(x) = \frac{N}{\mu} \exp\left(-\frac{x}{\mu}\right)$$

Where *N* is the total number of RTS centres and μ is the mean of the largest RTS amplitude in a pixel which, at 23°C, was found to be (0.19±0.03) fA and not a function of fluence or proton energy. It was suggested that this represented a universal maximum RTS amplitude but more work is required for confirmation. However, it is consistent, within experimental uncertainties, with a figure of 0.4 fA at 23°C, extrapolated from data at -5°C presented by Nuns et al. [91] on proton and neutron irradiated CCDs. In the same work the temperature dependence for 10 MeV proton irradiated devices was found to follow an $\exp(-E_a/kT)$ dependence with an E_a of 0.44 eV, although other reports give an E_a around 0.5 – 0.6 eV (e.g. [92]). Because of the low activation energy of the process it was assumed in [91] that the RTS generation could be attributed to high field zones. However, the RTS amplitudes seen in the devices tested in [32] showed no field dependence over the range of fields investigated. Early work on the STAR250 CMOS sensor, investigated in [93], showed that most RTS amplitudes were below 0.1 nA/cm^2 at 27°C, corresponding to a defect generation rate of 0.6 fA, also consistent with the more recent studies. In this work these RTS events were on top of a dark signal pedestal that appeared to be affected by field enhancement but the events themselves were not.

RTS defects generated by room temperature proton irradiation have shown similar annealing behaviour to the mean dark signal [73]. In [74] it was noted that a two hour, 50°C bake converted many of the multiple level RTS pixels to 2 level RTS pixels. A detailed annealing study [94] investigating the total number of RTS pixels showed the annealing behaviour was similar to that of the Si-E centre, but the phosphorous complex is not the only candidate for the RTS behaviour, especially as RTS phenomena is not limited to silicon devices.

If an RTS pixel has just two distinct levels of dark signal the time spent in the high or low dark signal states are randomly distributed but the average times in each state are well defined. It was noted in [74] that a small fraction of RTS pixels can have either very long or very short time constants and they can vary by up to four orders of magnitude, from seconds to hours, at room temperature. However, most have a time constant of a few minutes at room temperature. The time constant for each state of the RTS defect has been found to have the form [92]

$$\frac{1}{\tau} = R \cdot \exp\left(\frac{-E}{kT}\right)$$

where the *R* is a constant. Many authors have measured the energy, *E*, to be around 0.9 eV. A lower activation energy value has been presented in [85] and this has been attributed tentatively to the fact that the CMOS device was operated in soft reset mode so lag may have affected the measurements [74].

Further work is required to fully characterise the RTS phenomena in silicon devices. For example detailed understanding of the temperature dependence of the RTS amplitude is lacking, as is the understanding and characterisation of the distribution of the time constants. However, it is clear that as temperature is lowered the transition amplitudes reduce and the switching time constants increase to such an extent that, if a silicon device is operated cold, for example at -50^{o}C, the effect of the RTS defects on mission performance can be insignificant. However, the generation of RTS defects in MCT and InGaAs imagers, even when operating cold, can be important.

An increase in the number of RTS pixels in InGaAs detectors has been reported in, for example [8]. Here the RTS amplitude was found not to correlate with high dark signal pixels, in common with silicon devices. In the same work the amplitudes were found to have an activation energy around 0.35 eV but an RTS pixel with a significantly lower activation energy was observed also. However, very little work on the detailed characteristic of RTS behaviour in infrared technologies has been published within the public domain and more work is required in this area.

A6.3.4 Charge Transfer Efficiency

The charge transfer efficiency (CTE) of a CCD is usually defined as the fraction of the signal remaining following the transfer of signal from one pixel to the next. Sometimes it is defined as the fraction of charge remaining on transfer from one phase to the next so care must be taken when interpreting published results. The CTE is an important parameter for CCDs. For surface channel CCDs[4] it is dominated by trapping by Si/SiO_2 interface states, so these devices are particularly sensitive to total ionising dose deposition. Most space missions utilise buried channel CCDs where signal charge does not come into contact with interface states so, not only is the CTE significantly better than surface channel devices, it is not affected by total ionising dose. However, as charge transfer takes place in the bulk silicon, CTE is degraded by displacement damage and the generation of discrete trapping centres.

A degraded CTE can have a significant impact on the performance of the instrument. The observed image degradation due to a loss of CTE is a strong function of the operating conditions of the CCD and the type of image being observed. The effect of CTE degradation on the performance of star trackers has been investigated in [95]. However, it is not possible to quote a single figure for the CTE degradation that covers all operating conditions, image types and CCD structures. Measured CTE figures are only directly relevant to the device type under test, running under the test operating conditions and with the images used for the test measurement. Therefore, to estimate the degradation that will be observed in practice it is necessary to understand the theory behind charge trapping and how the distributed signal within the CCD interacts with the traps. The theories are covered in detail within the quoted references. However, the main elements are presented here to illustrate the type of degradation to be expected. It was noted in [96] that it is probably not possible to predict effects to better than a factor two to three from published data because of variations in the operating conditions and the measurement techniques used in a given laboratory. For these reasons it was recommended that, for critical space applications, ground testing, tailored to reflect the in-orbit conditions as close as possible, be carried out.

As noted in section A6.1 the displacement damage generates traps that trap and emit electrons from the conduction band in the case of n-channel CCDs, or holes from the valence band in the case of p-channel CCDs. The trap species of importance is dependent on the operating conditions, and the temporal dynamics of trapping and emission, which depends on the nature of the trap. The Si-E centre and the deep acceptor state of the divacancy tend to dominate when operating n-channel CCDs warm. At colder temperatures the oxygen vacancy complex and the shallower state of the divacancy may become significant, and there are other, as yet unidentified defect species that can dominate the degradation observed at intermediate temperatures.

Despite the complication of the interactions with the generated defects, it has been found that the CTE degradation scales with NIEL, independent of particle type and energy, at least to a first approximation. However, divacancy production is not significant in electron irradiated devices but is important in proton irradiated devices. The CTE degradation is linearly dependent on the generated trap density. There is actually very little information in the literature on the introduction rate of the important defects especially that

[4] surface channel CCDs have been proposed for use in TDI earth observation missions where full well capacity is an important requirement.

of the Si-E centre for phosphorous concentrations typically used for the buried channel of n-channel CCDs. Therefore, to get suitable inputs for any modelling activity one must rely on measurements made on the CCDs directly. Unfortunately, the calculation of the density of the radiation induced traps requires a detailed knowledge of the charge distribution within a pixel and is therefore not straight forward. Using the concept of 'effective signal density' together with 1d device modelling, work performed in [11] and [12] on high energy electron irradiated CCDs estimated the introduction rate of the Si-E centre to be

$$N_t\,(\mathrm{cm}^{-3}) = (2.0 \pm 0.6) \times \mathrm{NIEL}\,(\mathrm{keVcm}^{-2}/\mathrm{g}) \times \Phi\,(\mathrm{cm}^{-2})$$

where Φ is the particle fluence. The defects produced by proton irradiation are dominated by the introduction of the Si-E centre but the divacancy is also important. Work published in [37] on 3 MeV proton irradiated devices, following detailed 2d modelling of the signal distribution, estimated an introduction rate of the Si-E centre as

$$N_t\,(\mathrm{cm}^{-3}) = 2.5 \times \mathrm{NIEL}\,(\mathrm{keVcm}^{-2}/\mathrm{g}) \times \Phi\,(\mathrm{cm}^{-2})$$

And for the divacancy

$$N_t\,(\mathrm{cm}^{-3}) = 0.4 \times \mathrm{NIEL}\,(\mathrm{keVcm}^{-2}/\mathrm{g}) \times \Phi\,(\mathrm{cm}^{-2})$$

In another study on 10 MeV proton irradiated devices [97] the density of a trap that could be attributed to the Si-E centre was found to have an introduction rate of

$$N_t\,(\mathrm{cm}^{-3}) = 1.1 \times \mathrm{NIEL}\,(\mathrm{keVcm}^{-2}/\mathrm{g}) \times \Phi\,(\mathrm{cm}^{-2}).$$

However, it should be noted that a very rough approximation for the charge density was used in [37] and thus the errors in the determination of the trap density could be large. A trap that may possibly be attributed to the divacancy was found to have an introduction rate of about 25% of that of the Si-E centre whilst a trap that may be the Si-A centre was introduced at about twice the rate of the Si-E centre. It is known that the introduction rate of the Si-A centre is dependent on the oxygen concentration within the silicon, which will vary depending on the source and type of silicon wafer. Several authors have reported the presence of a defect having an energy level around 0.3 eV below the conduction band edge which might be attributable to a carbon related complex but this is uncertain.

The basic theory of charge trapping has been discussed by many authors and will be covered here to illustrate the main points of CTE degradation. Since the signal is transferred in the depletion region, the only important mechanisms in n-channel CCDs are capture of signal electrons from the conduction band and their subsequent emission back to the conduction band from the trapping centre.

The time constants for the capture (τ_c) and emission (τ_e) processes are

$$\tau_c = 1/(\sigma_n v_{th} n_s)$$
$$\tau_e = \exp(E/kT)/(\sigma_n X_n v_{th} N_c \chi)$$

Where

n_s	=	signal density
σ_n	=	electron capture cross section
v_{th}	=	mean thermal velocity for electrons
N_c	=	effective density of states in the conduction band
T	=	Temperature
k	=	Boltzmann's constant
X_n	=	'entropy factor'
χ	=	field enhancement factor
E	=	energy level of the trap below the conduction band edge

The field enhancement factor was added in [98] to allow for possible increased emission rates in high field regions of the device. In practice χ was found to be very close to unity. The traps are characterised by their energy level within the band gap, capture cross section and its degeneracy. These parameters are often assessed using transient techniques such as deep level transient spectroscopy (DLTS) but can also be measured using the CCD itself. However, experimental difficulties and uncertainties lead to a range of published values. This is quite unfortunate as the emission time constant is exponentially dependant on the energy level and small uncertainty in the determination of the energy level will lead to significant errors in the emission time constant. For the following illustrations tentative trap parameters following 5×10^9 10 MeV protons/cm^2 are presented in Table 2. There will be other low level defects generated that result in relevant trapping and emission as found in, for example, [99] and parameters for an “unknown” defect having an energy level 0.31 eV below the conduction band edge is also included.

Table 2 Tentatively assigned defect parameters following 5×10^9 10 MeV protons/cm^2

	Si-E	$(V\text{-}V)^-$	$(V\text{-}V)^{--}$	Si-A	Unknown
N_t (cm^{-3})	1×10^{11}	1.5×10^{10}	1.5×10^{10}	2×10^{11}	5×10^{9}
E_c-E_t (eV)	0.46	0.41	0.21	0.17	0.31
$\sigma_n X$ (cm^2)	6×10^{-15}	5×10^{-15}	5×10^{-16}	1×10^{-14}	3×10^{-16}

The emission time constants for traps having the parameters in Table 2 are presented in Figure 31.

Once the radiation induced trap population is known the effects on the CTE degradation can be calculated. A full and rigorous treatment requires a 3d device simulation of the CCD structure to account for the signal distribution and a Monte Carlo approach can be taken to track the interaction with the traps. Such a simulation is being developed [100] but it does require significant computational resource and an intimate understanding of the pixel architecture which is not always available from the manufacturer. Empirical and semi empirical models have been developed but a simple analytical approach is given here to illustrate the main points.

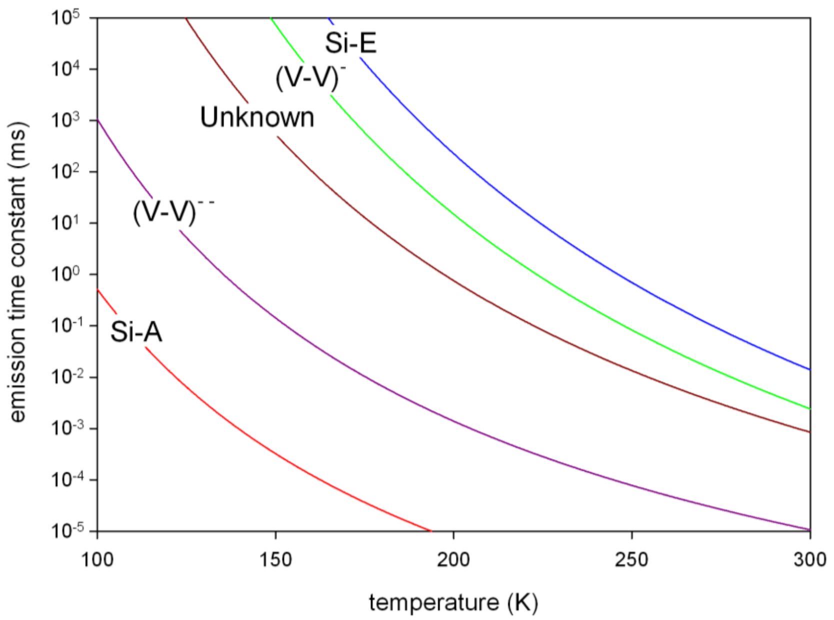

Figure 31 Approximate values for the emission time constants of the defects mainly responsible for CTE degradation in n-channel CCDs.

First emission of charge from the traps is considered. When a charge packet is present in a pixel a number of electrons, s_t, will be trapped within the pixel volume. If the charge packet is transferred from this pixels, and no other charge packet follows, then s_t decreases such that

$$\frac{ds_t}{dt} = -\frac{s_t}{\tau_e}$$

i.e.

$$s_t = s_{t0} \exp(-t/\tau_e)$$

If another charge packet, the same size as the first, is transferred to the pixel, the number of electrons trapped and lost from this charge packet will now be

$$s_{lost} = s_{t0}(1 - \exp(-t_0/\tau_e))$$

where t_0 is the time between charge packets passing through the same pixel. Thus, if the time between charge packets is very much less than the emission time constant of the trap, the traps would not have emitted the charge captured from the previous charge packet and therefore do not contribute to the reduction in the apparent CTE. This is illustrated in Figure 32 which shows the effect of the Si-E centre having parameters shown in Table 2. The plot can be thought of as a normalised charge transfer inefficiency (CTI) where the CTI is defined as 1 - CTE. As the time between bursts of signal decreases, less time is available for the traps to emit their charge. Therefore the low temperature side of the peak shifts towards higher temperatures where the emission time constant is reduced. In x-ray spectroscopic applications, for example, the data is very sparse and t_0 can be quite long. Therefore, to minimise the CTE degradation and thus optimise the spectroscopic resolution, the CCD must be cooled so the traps remain filled for long periods of time. It is not unusual, in these situations, to run the CCD at temperatures around 180K. Work performed in [101] studied the effect of x-ray hit rate, and thus effectively t_o, for the XMM mission.

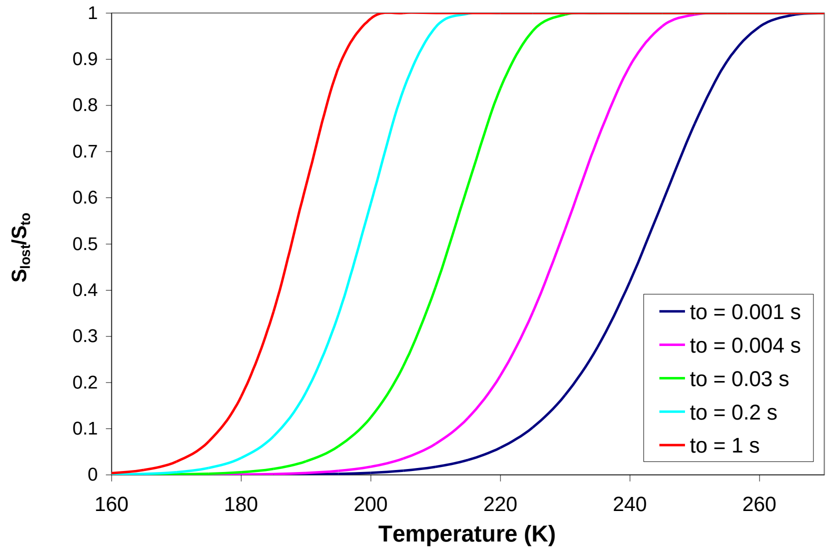

Figure 32 Calculated s_{lost}/s_{t0} for various times between charge packets.

If the emission time constant is very much shorter than the clock period then the electrons, if trapped, can be re-emitted back into the signal, thus reducing the CTI. To illustrate this effect it is necessary to consider when charge can be re-emitted back into the signal. This will be dependent on the clock timings employed. One possible clock sequence for a 3-phase device is shown in Figure 33.

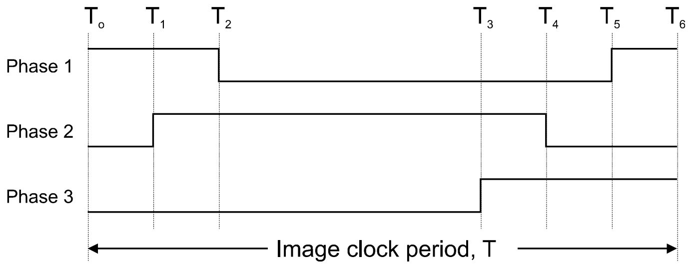

Figure 33 A typical clock sequence for a 3-phase CCD.

The resultant transfer of charge from one pixel to the next is shown in Figure 34. During the first period charge is being integrated under Phase 1. When charge transfer commences the signal is shared between Phase 1 and Phase 2. The reduction of signal under Phase 1 exposes depleted silicon previously occupied by signal charge. Thus trapped charge in this region will start to emit. However, for simplicity, this will be ignored in the following analysis. During period 3 the signal charge is wholly confined under Phase 2. A fraction of the charge that has been trapped under Phase 1 will now re-emit back into the signal during time $T_3 - T_2$. On commencement of the next transfer the signal charge will be shared between Phase 2 and Phase 3. Roughly half the charge that was trapped under Phase 1 and emitted in time period $T_4 - T_3$ will rejoin the signal charge packet. This charge capture and emission continues as the charge is transferred to the next pixel. The total signal rejoining the main packet after being trapped under Phase 1 is

$$s_{join} = \frac{s_{t0}}{2}\left(2 - \exp\left(-\frac{T_3 - T_2}{\tau_e}\right) - \exp\left(-\frac{T_4 - T_2}{\tau_e}\right)\right)$$

Therefore the total signal lost on passing through Phase 1 is simply

$$s_{total\phi 1} = s_{lost} - s_{join} = s_{t0}\left(1 - \exp\left(-\frac{t_0}{\tau_e}\right)\right) - \frac{s_{t0}}{2}\left(2 - \exp\left(-\frac{T_3 - T_2}{\tau_e}\right) - \exp\left(-\frac{T_4 - T_2}{\tau_e}\right)\right).$$

Similar expressions can be obtained for passing through Phase 2 and Phase 3. The results must be summed to get s_{total}, the total charge lost from the charge packet on moving from one pixel to the next.

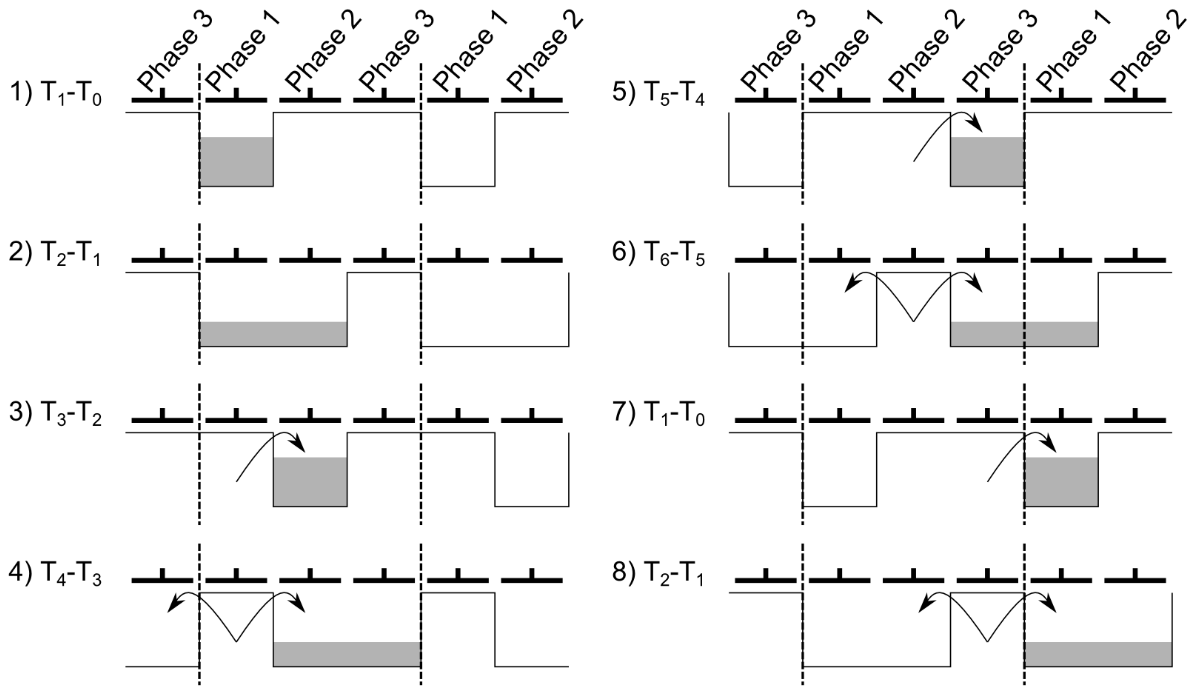

Figure 34 The return of trapped signal to the charge packet

The signal is distributed within the pixel and the signal density is not uniform. However, to illustrate the effect of trap capture and emission we can look at a small volume of the charge packet such that

$$\delta s_{t0} = N_t \delta V_s$$

Where δV_s is the volume occupied by the trapped signal δs_{to}. Figure 35 shows the result of the calculation of $\delta s_{total}/\delta V_s$ utilising the clock timings of Table 3, which are typical of the parallel clocks for time delay and integrate (TDI) operation.

Table 3 The clock timings (in µs) used to generate Figure 35.

T2-T1	T3-T2	T4-T3	T5-T4	T6-T5	T
5	5	5	5	5	1000

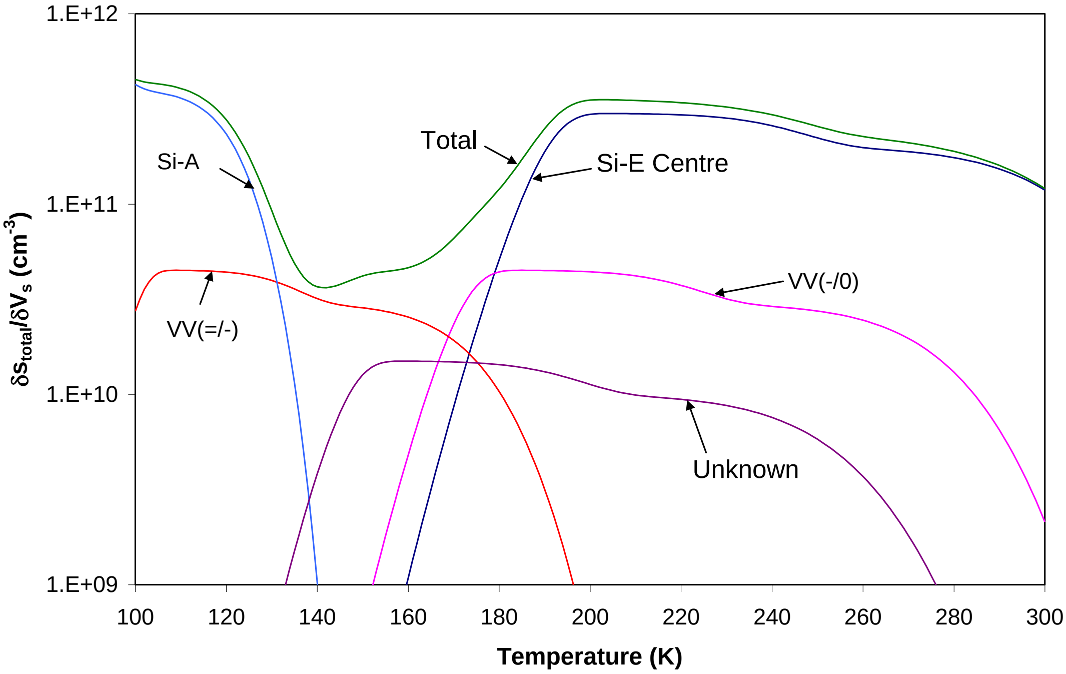

Figure 35 The effect of the different trap species on the CTI of an n-channel CCD. The clock timings employed in the calculations are given in Table 3. A t_o of 1 second is used here for illustration.

We need to look at the trapping process itself to complete the picture of signal loss. If charge is transferred to a gate having empty bulk traps, the traps will fill so that, after a time t_g, the density of filled traps will be

$$n_t = \frac{N_t \tau_e}{\tau_c + \tau_e}\left(1 - \exp\left(-t_g\left(1/\tau_c + 1/\tau_e\right)\right)\right)$$

where N_t is the trap density. Therefore, if the time the signal spends under a gate is comparable to or less than the capture time constant incomplete trapping will be observed.

To calculate the total amount of trapped signal the distribution of signal within the pixel needs to be considered as the capture time constant is dependent on the signal density. The calculation would be straight forward if the signal electrons are confined to a well-defined volume, throughout which the signal density, and thus the probability of capture is constant. This is not the case and the density varies throughout the volume of the charge packet as illustrated in Figure 36.

An “effective” signal density can, however, be defined. This is a strong function of signal size, increasing with increasing number of electrons in the signal. Thus the CTI can be considerably higher for small signals than observed with larger signals. For example, the effective signal density for the readout register of an EEV CCD01 (register pixel size = 22 µm x 88 µm) was measured to be 3 10^{13} cm^{-3} for a signal size of 500 electrons, increasing to about 2.5 10^{14} cm^{-3} for a signal size of 70,000 electrons [11, 12].

By confining the signal to smaller volumes the effective signal density increases. This has the effect of reducing the number of traps with which the charge packet can interact. This is the principle behind the use of a supplementary buried channel (notch) which can be effective in reducing the CTE degradation for small signals. However, increasing the effective signal density reduces the capture time constant which may adversely affect the CTI, dependent on the clocking frequencies used.

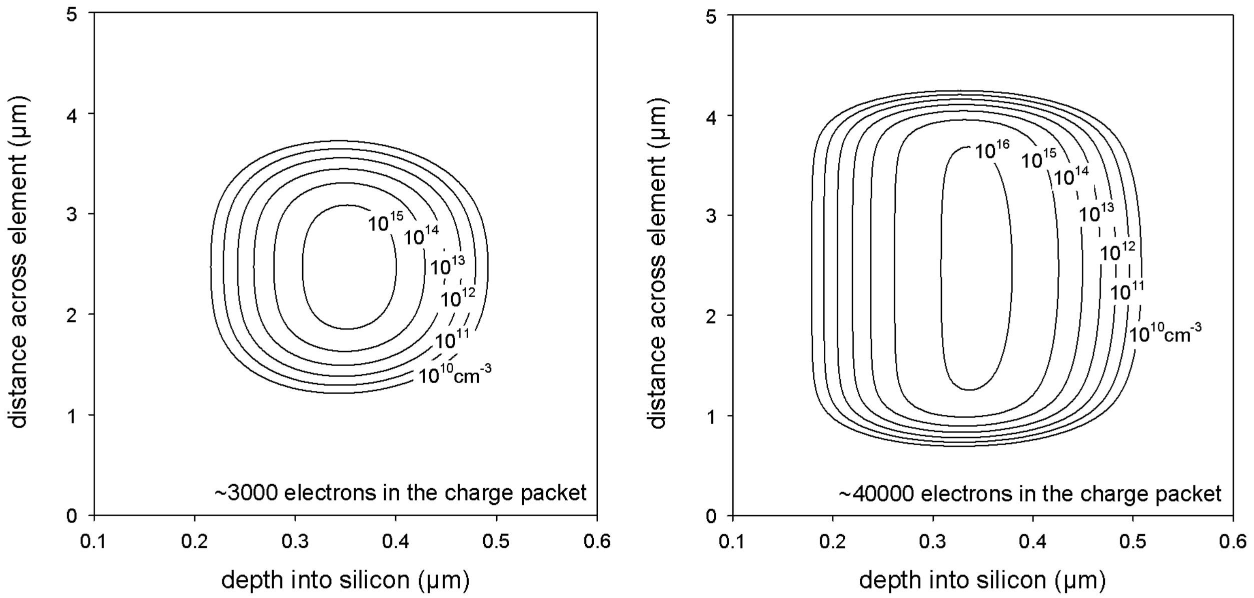

Figure 36 Calculated 2d signal distributions for signal under a 5 µm gate of a typical CCD having a 15 µm square pixel

Background signal can improve the CTI due to the filling of traps and the increase in signal density of the charge packet. When estimating the CTI with a background signal it is necessary to look at the charge distribution in detail and a full 3d device simulation is required for a rigorous analysis.

At operation around room temperature displacement damage induced charge transfer inefficiency as been observed (for example [11] and [73]) and to reduce by annealing at temperatures around 150^{o}C and it is likely that the breakup of the Si-E centre (phosphorous-vacancy complex) is responsible.

A CCD, manufactured on high resistivity silicon, irradiated with 120-keV protons while at a temperature of -100 ^{o}C has shown a significant increase (reverse annealing) in CTI following warm up to +30^{o}C and cool back down to -100 ^{o}C [102]. However, this CTI annealing behaviour has not been observed in the proton and alpha particle irradiated devices tested by Hopkinson et al. ([6] and [7]). Under these temperatures and operating conditions it is likely that the CTI degradation observed in these cases is impurity related, by, for example, the introduction of defects involving carbon. As impurity densities are likely so vary from manufacturer to manufacturer, and even wafer to wafer, the damage observed and the annealing behaviour it likely to show variability when a device is operated cold.

The previous discussions have been based around the degradation of n-channel CCDs. P-channel devices may offer improved radiation tolerance under certain conditions due to the significantly lower density of phosphorous and thus lower introduction rate of the Si-E centre and have been studied in, for example [103] and [104]. Work performed in [104] has indicated that, although the CTE in the pre irradiated devices tested was worse than in n-channel devices the rate of degradation was lower, providing an improved end of life performance.

A6.4 Responsivity Degradation

Total ionising dose deposition can cause responsivity changes due to threshold shifts of FETs used in the output amplifiers of silicon devices or ROICs, thus causing a change in the amplifier gain. Conversely, for typical displacement damage doses experienced in the space environment, displacement damage should not cause a significant change in the gain of these amplifiers. However, the responsivity of LWIR HgCdTe imagers has been found to degrade with proton fluence [105]. This degradation was attributed to the reduction in lateral diffusion length following displacement damage. The effect this has on the response of the image depends on the design of the diode structure and the reliance on lateral diffusion for charge collection. This behaviour has been seen also in Type II superlattice infrared detectors [106] and also silicon pn diode structures [107].

REFERENCES

[1] T. Beutier, J. Alozy, R. W. Ostedrof, S. Brabdnburg, G. Rolland, R.Ecoffet, “Experimental Simulator of Space Environment Proton Fluences”, RADECS Workshop 27th-29th Sept 2006, Athens, Greece

[2] The Stopping and Range of Ions in Matter, SRIM, http://www.srim.org/

[3] Hallen, A.; Fenyo, D.; Sundqvist, B. U. R.; Johnson, R. E.; Svensson, B. G.; , "The influence of ion flux on defect production in MeV proton irradiated silicon," Journal of Applied Physics , vol.70, no.6, pp.3025-3030, Sep 1991

[4] Leveque, P; Hallen, A; Pellegrino, P; Svensson, BG; Privitera, V. ,“Dose-rate influence on the defect production in MeV proton-implanted float-zone and epitaxial n-type silicon” Nuclear Instruments & Methods in Physics Research Section B Jan, 2002; 186; p375-p379

[5] Dale, C.J.; Chen, L.; McNulty, P.J.; Marshall, P.W.; Burke, E.A.; , "A comparison of Monte Carlo and analytic treatments of displacement damage in Si microvolumes," Nuclear Science, IEEE Transactions on, vol.41, no.6, pp.1974-1983, Dec. 1994

[6] Hopkinson, G.R.; Gare, P.; Sarri, G.; , "Effects of Low Temperature Proton Irradiation on a Large Area CCD for Astrometric Applications," Nuclear Science, IEEE Transactions on , vol.57, no.4, pp.2035-2043, Aug. 2010

[7] Hopkinson, G. R.; Mohammadzadeh, A.; , "CCD Radiation Testing at Low Temperatures Using a Laboratory Alpha Particle Source," Nuclear Science, IEEE Transactions on , vol.53, no.6, pp.3758-3763, Dec. 2006

[8] Barde, S.; Ecoffet, R.; Costeraste, J.; Meygret, A.; Hugon, X.; , "Displacement damage effects in InGaAs detectors: experimental results and semi-empirical model prediction," Nuclear Science, IEEE Transactions on , vol.47, no.6, pp.2466-2472, Dec 2000

[9] Susana MARTÍN BARBERO, Stefan K. HÖFFGEN, Guy BERGER, Héctor GUERRERO, “Compendium of International Irradiation Test Facilities” RADECS 2011

[10] A. B. Smith, P. R. Fields, J. H. Roberts, “Spontaneous Fission Neutron Spectrum of Cf^{252}”, Phys. Rev. 108, 411–413 (1957)

[11] Robbins, M.S.; Roy, T.; Watts, S.J.; , "Degradation of the charge transfer efficiency of a buried channel charge coupled device due to radiation damage by a beta source," Radiation and its Effects on Devices and Systems, 1991. RADECS 91., First European Conference on , vol., no., pp.327-332, 9-12 Sep 1991

[12] Robbins, M.S.; “Radiation Damage Effect in Charge Coupled Devices”, PhD Thesis, Brunel University, 1992

[13] Joseph J . Devar, “ The beta spectra of ^{90}Sr and ^{90}Y”, Los Alamos Report LA-10467-MS, Issued August 1985

[14] Colerico, C.W.; Serreze, H.B.; Messenger, S.R.; Xapsos, M.A.; Burke, E.A.; , "Alpha particle simulation of space radiation damage effects in semiconductor devices," Nuclear Science, IEEE Transactions on , vol.42, no.6, pp.2089-2094, Dec 1995

[15] Hopkinson, G.R.; Mohammadzadeh, A.; , "Low Temperature Alpha Particle Irradiation of a STAR1000 CMOS APS," Nuclear Science, IEEE Transactions on , vol.55, no.4, pp.2229-2234, Aug. 2008

[16] Tivarus, C.; McColgin, W.C.; , "Dark Current Spectroscopy of Irradiated CCD Image Sensors," Nuclear Science, IEEE Transactions on , vol.55, no.3, pp.1719-1724, June 2008.

[17] McMahan, M.A.; Blackmore, E.; Cascio, E.W.; Castaneda, C.; von Przewoski, B.; Eisen, H.; , "Standard Practice for Dosimetry of Proton Beams for use in Radiation Effects Testing of Electronics," Radiation Effects Data Workshop, 2008 IEEE , vol., no., pp.135-141, 14-18 July 2008

[18] E. W. Cascio, and B. Gottschalk, “A Simplified Vacuumless Faraday Cup for the Experimental Beamline at the Francis H. Burr Proton Therapy Center”, Proc IEEE 2009 Radiation Effects Data Workshop, pp.161-165, 2009

[19] M. J. Selwood and S. D. Monk, “Construction Issues Surrounding a Portable Four-Band Neutron Detection System”, Radiation Protection Dosimetry (2011), Vol. 144, No. 1-4, pp. 249-252

[20] Harboe-Sorensen, R.; Guerre, F.-X.; Roseng, A.; , "Design, Testing and Calibration of a "Reference SEU Monitor" System," Radiation and Its Effects on Components and Systems, 2005. RADECS 2005. 8th European Conference on , vol., no., pp.B3-1-B3-7, 19-23 Sept. 2005

[21] ASTM Guidelines: E798-96 Standard practice for conducting irradiations at accelerator-based sources

F1190-99 Standard guide for neutron irradiation of unbiased electronic components
F980M-96 Standard guide for measurement of rapid annealing of neutron-induced displacement damage in silicon semiconductor devices

[22] Spezzigu, P.; Caddeo, C.; Quadri, G.; Gilard, O.; Bechou, L.; Ousten, Y.; Vanzi, M.; , "Implementation of a “Design of Experiments” Methodology for the Prediction of Phototransistor Degradation in a Space Environment," *Nuclear Science, IEEE Transactions on* , vol.56, no.4, pp.2465-2472, Aug. 2009

[23] ECSS, “Methods for the calculation of radiation received and its effects, and a policy for design margins” ECSS-E-ST-10-12C 15 November 2008

[24] Gordon R. Hopkinson; Teresa M. Goodman; Stuart R. Prince “A Guide to the Use and Calibration of Detector Array Equipment”, SPIE Society of Photo-Optical Instrumentation Engi; illustrated edition (Aug 2004) ISBN 0819455326

[25] Bedabrata Pain and Bruce R. Hancock, "Accurate estimation of conversion gain and quantum efficiency in CMOS imagers", Proc. SPIE 5017, 94 (2003)

[26] James R. Janesick, “Photon Transfer” SPIE Press; illustrated edition edition (2007), ISBN 0819467227

[27] R. C. Alig and S. Bloom, “Electron-Hole-Pair Creation Energies in Semiconductors”, Phys. Rev. Lett. 35, 1522–1525 (1975)

[28] A Owens, G.W Fraser, A.F Abbey, A Holland, K McCarthy, A Keay, A Wells, “The X-ray energy response of silicon (B): Measurements”, Nuclear Instruments and Methods in Physics Research Section A: Accelerators, Spectrometers, Detectors and Associated Equipment, Volume 382, Issue 3, 21 November 1996, Pages 503-510

[29] G.W. Fraser, A.F. Abbey, A. Holland, K. McCarthy, A. Owens, A. Wells, “The X-ray energy response of silicon Part A. Theory”, Nuclear Instruments and Methods in Physics Research Section A: Accelerators, Spectrometers, Detectors and Associated Equipment, Volume 350, Issues 1–2, 15 October 1994, Pages 368–378

[30] http://ie.lbl.gov/toi/nuclide.asp?iZA=480109

[31] Ori Fox, Augustyn Waczynski, Yiting Wen, Roger D. Foltz, Robert J. Hill, Randy A. Kimble, Eliot Malumuth and Bernard J. Rauscher, “The 55Fe x-ray energy response of mercury cadmium telluride near-infrared detector arrays”, Proc. SPIE 7021, 702123 (2008);

[32] Goiffon, V.; Hopkinson, G.R.; Magnan, P.; Bernard, F.; Rolland, G.; Saint-Pe, O.; , "Multilevel RTS in Proton Irradiated CMOS Image Sensors Manufactured in a Deep Submicron Technology," Nuclear Science, IEEE Transactions on , vol.56, no.4, pp.2132-2141, Aug. 2009

[33] Waczynski, A.; Polidan, E.J.; Marshall, P.W.; Reed, R.A.; Johnson, S.D.; Hill, R.J.; Delo, G.S.; Wassell, E.J.; Cheng, E.S.; , "A comparison of charge transfer efficiency measurement techniques on proton damaged n-channel CCDs for the Hubble Space Telescope Wide-Field Camera 3," Nuclear Science, IEEE Transactions on , vol.48, no.6, pp.1807-1814, Dec 2001

[34] Mohsen, A.M.; Tompsett, M.F.; , "The effects of bulk traps on the performance of bulk channel charge-coupled devices," Electron Devices, IEEE Transactions on , vol.21, no.11, pp. 701- 712, Nov 1974

[35] Collet, M.G.; , "The influence of bulk traps on the charge-transfer inefficiency of bulk charge-coupled devices," Electron Devices, IEEE Transactions on , vol.23, no.2, pp. 224- 227, Feb 1976

[36] J.Janesick, G.Soli, T.Elliot, S.Collins, “The effects of proton damage on charge-coupled devices,” Proc.SPIE, 1991,vol.1447, pp.87–108.

[37] Hardy, T.; Murowinski, R.; Deen, M.J.; , "Charge transfer efficiency in proton damaged CCD's," Nuclear Science, IEEE Transactions on , vol.45, no.2, pp.154-163, Apr 1998

[38] J.A. Gregory, B.E. Burke and M.J. Cooper, Solid State Research, Quarterly Technical Report (ESC-TR-92-149), Lincoln Laboratory, MIT, 31 Jan 1993, pp. 48-50

[39] ECSS “Space Environment” ECSS-E-10-04C 2008

[40] Janet Barth, “Modelling Space Radiation Environments,” Notes from the 1997 IEEE Nuclear and Space Radiation Effects Conference Short Course, Snowmass CO (1997)

[41] Eamonn Daly, “Space Weather and Radiation Effects from Space to Ground,” Notes from the RADECS2001 Short Course, Grenoble, France (2001)

[42] Insoo Jun; Garrett, H.B.; Evans, R.W.; , "High-energy trapped particle environments at Jupiter: an update," *Nuclear Science, IEEE Transactions on* , vol.52, no.6, pp. 2281- 2286, Dec. 2005

[43] SPENVIS, The Space Environment Information System - http://www.spenvis.oma.be/
[44] OMERE, http://www.trad.fr/OMERE-Software.html
[45] SPACE RADIATION, http://www.spacerad.com/
[46] Truscott, P.; Fan Lei; Dyer, C.; Quaghebeur, B.; Heyndericks, D.; Nierninen, P.; Evans, H.; Daly, E.; Mohammadzadeh, A.; Hopkinson, G.; , "Mulassis - monte carlo radiation shielding simulation for space applications made easy," Radiation and Its Effects on Components and Systems, 2003. RADECS 2003. Proceedings of the 7th European Conference on , vol., no., pp.191-196, 15-19 Sept. 2003
[47] James R. Janesick, “Fundamentals of Scientific Charge-coupled Devices”, SPIE Publications, ISBN 0819436984, 2001.
[48] A.J. Theuwissen, “Solid-State Imaging with Charge-Coupled Devices”, Springer, ISBN 0792334566, 1996.
[49] Kozlowski, L. J. et al. ; “Low-noise infrared and visible focal plane arrays”, Opto-Electr. Rev., 7, n0. 4, pp 259-269, 1999
[50] James W. Beletic, Richard Blank, David Gulbransen, Donald Lee, Markus Loose, Eric C. Piquette, Thomas Sprafke, William E. Tennant, Majid Zandian and Joseph Zino, "Teledyne Imaging Sensors: infrared imaging technologies for astronomy and civil space", Proc. SPIE 7021, 70210H (2008)
[51] V.A.J. van Lint, T.M. Flanagan, R.E. Leadon, J.A. Naber, V.C. Rogers “Mechanisms of Radiation Effects in Electronic Materials”, John Wiley & Sons, 1980.
[52] Michael Moll “Radiation Damage in Silicon Particle Detectors. Microscopic and Macroscopic Properties”, PhD Thesis, Hamburg University, 1999.
[53] Messenger, G.C.; , "A summary review of displacement damage from high energy radiation in silicon semiconductors and semiconductor devices," *Nuclear Science, IEEE Transactions on* , vol.39, no.3, pp.468-473, Jun 1992
[54] Srour, J.R.; Marshall, C.J.; Marshall, P.W.; , "Review of displacement damage effects in silicon devices," Nuclear Science, IEEE Transactions on , vol.50, no.3, pp. 653- 670, June 2003
[55] Pickel, J.C.; Kalma, A.H.; Hopkinson, G.R.; Marshall, C.J.; , "Radiation effects on photonic imagers-a historical perspective," Nuclear Science, IEEE Transactions on , vol.50, no.3, pp. 671- 688, June 2003
[56] Watts, S.J.; Matheson, J.; Hopkins-Bond, I.H.; Holmes-Siedle, A.; Mohammadzadeh, A.; Pace, R.; , "A new model for generation-recombination in silicon depletion regions after neutron irradiation," Nuclear Science, IEEE Transactions on , vol.43, no.6, pp.2587-2594, Dec 1996
[57] Srour, J. R.; Palko, J. W.; , "A Framework for Understanding Displacement Damage Mechanisms in Irradiated Silicon Devices," *Nuclear Science, IEEE Transactions on* , vol.53, no.6, pp.3610-3620, Dec. 2006
[58] Inguimbert, C.; Arnolda, P.; Nuns, T.; Rolland, G.; , "“Effective NIEL” in Silicon: Calculation Using Molecular Dynamics Simulation Results," *Nuclear Science, IEEE Transactions on* , vol.57, no.4, pp.1915-1923, Aug. 2010
[59] Dale, C.J.; Chen, L.; McNulty, P.J.; Marshall, P.W.; Burke, E.A.; , "A comparison of Monte Carlo and analytic treatments of displacement damage in Si microvolumes," Nuclear Science, IEEE Transactions on, vol.41, no.6, pp.1974-1983, Dec. 1994
[60] Huhtinen, M.; Aarnio, P. A.; “Pion induced displacement damage in silicon devices”, Nuclear Instruments and Methods in Physics Research Section A, Volume 335, Issue 3, p. 580-582, 1993
[61] Akkerman A., et al. “Updated NIEL calculations for estimating the damage induced by particles and gamma rays in Si and GaAs”, Radiation Physics and Chemistry, vol. 62. pp. 301-331, 2001.
[62] Summers, G.P.; Burke, E.A.; Shapiro, P.; Messenger, S.R.; Walters, R.J.; , "Damage correlations in semiconductors exposed to gamma, electron and proton radiations," Nuclear Science, IEEE Transactions on , vol.40, no.6, pp.1372-1379, Dec 1993
[63] http://sesam.desy.de/members/gunnar/Si-dfuncs.html
[64] Walters, R.J.; Shaw, G.J.; Summers, G.P.; Burke, E.A.; Messenger, S.R.; , "Radiation effects in Ga0.47In0.53As devices ," Nuclear Science, IEEE Transactions on , vol.39, no.6, pp.2257-2264, Dec 1992
[65] Fodness, B.C.; Marshall, P.W.; Reed, R.A.; Jordan, T.M.; Pickel, J.C.; Insoo Jun; Xapsos, M.A.; Burke, E.A.; Ladbury, R.; , "Monte carlo treatment of displacement damage in bandgap engineered HgCdTe detectors," Radiation and Its Effects on Components and Systems, 2003. RADECS 2003. Proceedings of the 7th European Conference on , vol., no., pp.479-485, 15-19 Sept. 2003

[66] Insoo Jun; Xapsos, M.A.; Messenger, S.R.; Burke, E.A.; Walters, R.J.; Summers, G.P.; Jordan, T.; , "Proton nonionizing energy loss (NIEL) for device applications," Nuclear Science, IEEE Transactions on , vol.50, no.6, pp. 1924- 1928, Dec. 2003

[67] Insoo Jun; Wousik Kim; Evans, R.; , "Electron Nonionizing Energy Loss for Device Applications," *Nuclear Science, IEEE Transactions on* , vol.56, no.6, pp.3229-3235, Dec. 2009

[68] Inguimbert, C.; Gigante, R.; , "NEMO : a code to compute NIEL of Protons, neutrons, electrons and heavy ions," Radiation and Its Effects on Components and Systems, 2005. RADECS 2005. 8th European Conference on , vol., no., pp.PG2-1-PG2-8, 19-23 Sept. 2005.

[69] Inguimbert, C.; Gigante, R.; , "NEMO: A Code to Compute NIEL of Protons, Neutrons, Electrons, and Heavy Ions," Nuclear Science, IEEE Transactions on , vol.53, no.4, pp.1967-1972, Aug. 2006.

[70] Dale, C.J.; Marshall, P.W.; Burke, E.A.; Summers, G.P.; Bender, G.E.; , "The generation lifetime damage factor and its variance in silicon ," Nuclear Science, IEEE Transactions on , vol.36, no.6, pp.1872-1881, Dec 1989

[71] Robbins, M.S.; , "High-energy proton-induced dark signal in silicon charge coupled devices," Nuclear Science, IEEE Transactions on , vol.47, no.6, pp.2473-2479, Dec 2000

[72] Srour, J.R.; Lo, D.H.; , "Universal damage factor for radiation-induced dark current in silicon devices," Nuclear Science, IEEE Transactions on , vol.47, no.6, pp.2451-2459, Dec 2000

[73] Hopkinson, G.R.; Mohammadzadeh, A.; , "Comparison of CCD damage due to 10- and 60-MeV protons," Nuclear Science, IEEE Transactions on , vol.50, no.6, pp. 1960- 1967, Dec. 2003

[74] Hopkinson, G.R.; Goiffon, V.; Mohammadzadeh, A.; , "Random Telegraph Signals in Proton Irradiated CCDs and APS," Nuclear Science, IEEE Transactions on , vol.55, no.4, pp.2197-2204, Aug. 2008

[75] Shaw, G.J.; Messenger, S.R.; Walters, R.J.; Summers, G.P.; , “Radiation induced reverse dark currents in $In_{0.53}Ga_{0.47}As$ photodiodes,” J. Appl. Phys. 73, 7244 (1993)

[76] Kudou, T. et al.;, “Effect of irradiation in InGaAs photo devices,” Journal of Radioanalytical and Nuclear Chemistry, Vol. 239, No. 2 (1999) 361-364

[77] O. Amore, J. P. Bonifaci, Gianrossano Giannini, Xavier Hugon, S. Lacroix and Jean-Pierre Moy, "InGaAs SWIR imaging detectors hardening against proton irradiation", Proc. SPIE 4820, 436 (2003)

[78] Kleipool, Q. L.; Jongma, R. T.; Gloudemans, A. M. S.; Schrijver, H.; Lichtenberg, G. F.; van Hees, R. M.; Maurellis, A. N.; Hoogeveen, R. W. M.; , “In-flight proton-induced radiation damage to SCIAMACHY’s extended-wavelength InGaAs near-infrared detectors,” Infrared Physics & Technology, Volume 50, Issue 1, p. 30-37.

[79] Hopkinson, G.; Sorensen, R.H.; Leone, B.; Meynart, R.; Mohammadzadeh, A.; Rabaud, W.; , "Radiation Effects in InGaAs and Microbolometer Infrared Sensor Arrays for Space Applications," Nuclear Science, IEEE Transactions on , vol.55, no.6, pp.3483-3493, Dec. 2008

[80] Scott D. Johnson, Augustyn Waczynski, Paul W. Marshall, Elizabeth J. Polidan, Cheryl J. Marshall, Robert A. Reed, Randy A. Kimble, Gregory Delo, David Schlossberg, Anne Marie Russell, Terry Beck, Yiting Wen, John Yagelowich, Robert J. Hill, Edward Wassell and Edward S. Cheng, "Radiation effects in WFC3 IR detectors", Proc. SPIE 5167, 243 (2004)

[81] Weber, A.; Belzner, W.; Haas, L.-D.; Hanna, S.; Hofmann, K.; Neef, A.; Reder, M.; Stifter, P.; Wendler, J.; Ziegler, J.; Nothaft, H.-P.; , "Radiation hardness of two-dimensional focal plane detector arrays for LWIR/VLWIR space sounding missions," *Radiation and Its Effects on Components and Systems (RADECS), 2011 12th European Conference on* , vol., no., pp.336-339, 19-23 Sept. 2011

[82] Dale, C.J.; Marshall, P.W.; Burke, E.A.; , "Particle-induced spatial dark current fluctuations in focal plane arrays," Nuclear Science, IEEE Transactions on , vol.37, no.6, pp.1784-1791, Dec 1990

[83] Marshall, P.W.; Dale, C.J.; Burke, E.A.; "Proton-induced displacement damage distributions and extremes in silicon microvolumes charge injection device," Nuclear Science, IEEE Transactions on , vol.37, no.6, pp.1776-1783, Dec 1990

[84] P.W. Marshall, C.J. Dale, E.A. Burke, “Proton-induced displacement damage fluctuations in silicon microvolumes,” Nuclear Instruments and Methods in Physics Research Section B: Beam Interactions with Materials and Atoms, Volumes 56-57, Part 2, 1 May 1991, Pages 847-850

[85] Bogaerts, J.; Dierickx, B.; Mertens, R.; , "Enhanced dark current generation in proton-irradiated CMOS active pixel sensors," Nuclear Science, IEEE Transactions on , vol.49, no.3, pp. 1513- 1521, Jun 2002

[86] Gilard, O.; Boutillier, M.; Quadri, G.; Rolland, G.; Germanicus, R.; , "New Approach for the Prediction of CCD Dark Current Distribution in a Space Radiation Environment," *Nuclear Science, IEEE Transactions on* , vol.55, no.6, pp.3626-3632, Dec. 2008

[87] Gilard, O.; Boatella-Polo, C.; Dolado-Perez, J.-C.; Auvergne, M.; Quadri, G.; Boutillier, M.; , "CoRoT Satellite: Analysis of the In-Orbit CCD Dark Current Degradation," *Nuclear Science, IEEE Transactions on* , vol.57, no.3, pp.1644-1653, June 2010

[88] Marshall, C.J.; Marshall, P.W.; Howe, C.L.; Reed, R.A.; Weller, R.A.; Mendenhall, M..; Waczynski, A..; Ladbury, R..; Jordan, T.M.; , "Comparison of Measured Dark Current Distributions With Calculated Damage Energy Distributions in HgCdTe," Nuclear Science, IEEE Transactions on , vol.54, no.4, pp.1097-1103, Aug. 2007

[89] Goiffon, V.; Magnan, P.; Martin-Gonthier, P.; Virmontois, C.; Gaillardin, M.; , "Evidence of a Novel Source of Random Telegraph Signal in CMOS Image Sensors," *Electron Device Letters, IEEE* , vol.32, no.6, pp.773-775, June 2011

[90] Virmontois, C.; Goiffon, V.; Magnan, P.; Saint-Pe, O.; Girard, S.; Petit, S.; Rolland, G.; Bardoux, A.; , "Total Ionizing Dose Versus Displacement Damage Dose Induced Dark Current Random Telegraph Signals in CMOS Image Sensors," *Nuclear Science, IEEE Transactions on* , vol.58, no.6, pp.3085-3094, Dec. 2011

[91] Nuns, T.; Quadri, G.; David, J.-P.; Gilard, O.; Boudou, N.; , "Measurements of Random Telegraph Signal in CCDs Irradiated With Protons and Neutrons," Nuclear Science, IEEE Transactions on , vol.53, no.4, pp.1764-1771, Aug. 2006

[92] Hopkins, I.H.; Hopkinson, G.R.; , "Random telegraph signals from proton-irradiated CCDs," Nuclear Science, IEEE Transactions on , vol.40, no.6, pp.1567-1574, Dec 1993

[93] Bogaerts, J.; Dierickx, B.; Mertens, R.; , "Random telegraph signals in a radiation-hardened CMOS active pixel sensor," Nuclear Science, IEEE Transactions on , vol.49, no.1, pp.249-257, Feb 2002

[94] Nuns, T.; Quadri, G.; David, J.-P.; Gilard, O.; Annealing of Proton-Induced Random Telegraph Signal in CCDs," Nuclear Science, IEEE Transactions on , vol.54, no.4, pp.1120-1128, Aug. 2007

[95] Hopkinson, G.R.; , "Proton-induced changes in CTE for n-channel CCDs and the effect on star tracker performance," Nuclear Science, IEEE Transactions on , vol.47, no.6, pp.2460-2465, Dec 2000

[96] G R Hopkinson, C J Dale, P W Marshall "Proton effects in charge coupled devices" IEEE Trans Nucl Sci, Vol 43, 1996, 614-627

[97] Holland A. "The effect of bulk traps in proton irradiated CCDs," NIM A326, 335-343 (1993)

[98] I H Hopkins, G R Hopkinson and B Johlander "Proton-Induced Charge Transfer Degradation in CCDs for Near Room Temperature Applications" IEEE Trans Nucl Sci, Vol 41, 1994, 1984-1991

[99] Hopkinson, G.R.; , "Proton-induced CCD charge transfer degradation at low-operating temperatures," Nuclear Science, IEEE Transactions on , vol.48, no.6, pp.1790-1795, Dec 2001

[100] G. Seabroke, A. Holland, D. Burt, and M. Robbins "Silvaco ATLAS model of ESA's Gaia satellite e2v CCD91-72 pixels" Proc. SPIE, vol. 7742, 2010

[101] Watts S J, Holmes-Siedle A, Holland A "Further Radiation Evaluation of X-ray Sensitive Charge Coupled Devices for the XMM Telescope" Final Report on ESTEC Contract 8815/90/NL/LC(SC) 1995

[102] Bautz, M.; Prigozhin, G.; Kissel, S.; LaMarr, B.; Grant, C.; Brown, S.; , "Anomalous annealing of a high-resistivity CCD irradiated at low temperature," Nuclear Science, IEEE Transactions on , vol.52, no.2, pp. 519- 526, April 2005

[103] Cheryl J. Marshall, Paul W. Marshall, Augustyn Wacynski, Elizabeth Polidan, Scott D. Johnson and Art Campbell, "Comparisons of the proton-induced dark current and charge transfer efficiency responses of n- and p-channel CCDs", Proc. SPIE 5499, 542 (2004);

[104] J. Gow, N. J. Murray, A. D. Holland, D. Burt and P. Pool, "A comparative study of proton radiation damage in p- and n-channel CCDs", Proc. SPIE 7435, 74350F (2009);

[105] Hubbs, J.E.; Marshall, P.W.; Marshall, C.J.; Gramer, M.E.; Maestas, D.; Garcia, J.P.; Dole, G.A.; Anderson, A.A.; , "Lateral Diffusion Length Changes in HgCdTe Detectors in a Proton Environment," Nuclear Science, IEEE Transactions on , vol.54, no.6, pp.2435-2443, Dec. 2007

[106] Jackson, E.M. et al.; , "Radiation Damage in Type II Superlattice Infrared Detectors," Journal of Electronic Materials Volume 39, Number 7, 852-856, 2010

[107] Pedroza, Guillaume; Gilard, Olivier; Bourqui, Marie-Lise; Bechou, Laurent; Deshayes, Yannick; How, Lip Sun; Rosala, Francois, "Proton effects on low noise and high responsivity silicon-based photodiodes for space environment", Journal of Applied Physics, 105, 024513, 2009.